

Epitaxial growth in dislocation-free strained alloy films: Morphological and compositional instabilities

Zhi-Feng Huang* and Rashmi C. Desai†
*Department of Physics, University of Toronto,
 Toronto, Ontario, Canada M5S 1A7*

The mechanisms of stability or instability in the strained alloy film growth are of intense current interest to both theorists and experimentalists. We consider dislocation-free, coherent, growing alloy films which could exhibit a morphological instability without nucleation. We investigate such strained films by developing a nonequilibrium, continuum model and by performing a linear stability analysis. The couplings of film-substrate misfit strain, compositional stress, deposition rate, and growth temperature determine the stability of film morphology as well as the surface spinodal decomposition. We consider some realistic factors of epitaxial growth, in particular the composition dependence of elastic moduli and the coupling between top surface and underlying bulk of the film. The interplay of these factors leads to new stability results. In addition to the stability diagrams both above and below the coherent spinodal temperature, we also calculate the kinetic critical thickness for the onset of instability as well as its scaling behavior with respect to misfit strain and deposition rate. We apply our results to some real growth systems and discuss the implications related to some recent experimental observations.

I. INTRODUCTION

The techniques and technology related to fabricating large single crystals of elemental materials like silicon (Si) or compounds like gallium arsenide (GaAs) has been perfected for decades now. Polished wafers of such single crystalline semiconductor materials are now routinely used as substrates, on which a series of thin layers are grown to create a desired heterostructure. Thin films of increasing complexity are now being fabricated due to constraints on operating conditions and performance of electronic and optical devices.

When the growth of the superimposed material layers is based on the atomic pattern of the substrate underneath, as if it is the extension of substrate structure, then the process is referred to as an epitaxial growth. Heteroepitaxy is the technique in which a thin film of a different material is grown on a substrate (as for example in a layer growth of AlAs on GaAs), and in which the deposited layer has the same crystal orientation as the substrate. Many materials (especially III-V compounds), though composed of different atoms, have identical crystal structures and nearly identical lattice spacing. A match of lattice spacing is important in epitaxial growth since it can minimize and possibly eliminate local strains in the growing film, and thus produce good quality thin solid layers. For example, one can in principle lattice-match an InGaAsP quaternary alloy of appropriate composition to either InP or GaAs, and tailor-make a semiconductor film which will have the electronic band gap within the range between 0.8 eV and 1.7 eV.

Although the alloy composition can be tuned to obtain a desirable band gap, the resulting device is useful only if the alloy composition remains homogeneous. In a typical epitaxial growth technique like molecular beam epitaxy (MBE), the stability of the growing film can depend on many variables. The homogeneity of the growing film clearly depends on the surface mobility of the material being deposited, the substrate temperature T , and the deposition rate v . Further, different sized atoms that are being deposited to fabricate an alloy film induce stresses in the substrate which in turn affect the behavior on the surface. In fact, the process of epitaxial growth is a nonequilibrium phenomenon in which surface, interfacial and elastic energies along with surface diffusion and alloy segregation play active roles. During the nonequilibrium growth of alloy films, elastic stress may be relieved through nucleation of dislocations and other defects. Inhomogeneities can also arise on account of two potential instabilities, from which the generation of dislocations can be avoided and one can obtain high quality thin film materials. These are the morphological instability and alloy segregation instability.

Morphological instability^{1,2,3} can be understood through two features: A solid film adsorbate on a solid substrate creates a uniaxial stress, and the driving force for surface diffusion of matter is proportional to the local strain energy density. If a small corrugation occurs on the surface of a uniaxially strained solid, local strain energy concentration is created at its valleys. As a result diffusion of matter occurs along the surface from valleys to peaks of the corrugation. Valleys then deepen due to loss of mass which leads to a further increase of local strain energy driving the instability. Surface energy plays a stabilizing role here: as corrugations deepen, surface area increases which has an associated energy cost inhibiting the growth of instability.

The alloy segregation instability is driven by alloy thermodynamics.⁴ It is typically modelled by a Ginzburg-Landau type free energy (the order parameter ϕ is related to the binary alloy concentration) in which the quadratic term has

a coefficient proportional to $(T - T_c)$. This term changes sign for $T < T_c$ and leads to an instability which drives a homogeneous mixture to segregate. This mechanism is called spinodal decomposition and is applicable for not too asymmetric mixtures within the classical spinodal. For asymmetric mixtures between the spinodal and coexistence curves, the mixture is metastable and requires large amplitude fluctuations to segregate via a nucleation mechanism.

In this paper we consider strained film growth without nucleation, and assume the growing film to be a coherent, dislocation-free binary or pseudo-binary alloy. Stability of such films have been considered previously both theoretically^{5,6,7,8,9,10,11,12,13,14,15,16,17,18,19,20,21,22} and experimentally. The systems explored experimentally include SiGe^{23,24,25,26,27,28,29} and InGaAs.^{30,31,32,33,34,35,36,37} Other interesting experimental studies include: single component films (Ge on a Si substrate),³⁸ GaAs homoepitaxy,³⁹ self-organised GaAs islands,⁴⁰ etc.; but these are not as relevant here. Many of these experimental papers show that stressed growing films can develop non-planar morphologies without dislocations or nucleation, for both symmetric binary alloy films (50-50 mixture) as well as asymmetric films. The onset of instability is measured through a kinetic critical thickness h_c (film thickness at which surface roughness first appears), and the characteristic wavelength of the instability has also been determined by experiments.

Early theoretical work focused on explaining nonplanar surface morphologies through the competition between surface energy and elastic strain energy arising from lattice mismatch $\epsilon = (\bar{a}^f - a^s)/a^s$, where \bar{a}^f is the average bulk film lattice parameter and a^s is the substrate lattice spacing. The important effects due to composition dependence of the film lattice parameter a^f , represented by the solute expansion coefficient^{4,41} $\eta = (\partial a^f / \partial \phi) / a^f$ where ϕ is the local concentration field, were added in a kinetic treatment of the growing film.^{8,9,10,11,12,13,14,18,20} Intricate dependence on ϵ and η leads to sensitivity of the morphological development to the sign of the misfit ϵ , *i.e.* compressive and tensile regions of the growing film behave differently. Another important factor, the composition dependence of the elastic moduli, can also impact on the stability of the film and its sensitivity to the sign of ϵ .^{18,20} Experimental observations can provide a sensitive test of these theories in connection with the ϵ -asymmetry in the stability diagram of the growing film, the coupling between morphological instability and alloy segregation, as well as the behaviors of critical thickness.

An additional factor is the differing atomic mobilities of the two (or more) species on the growing film surface, and has been investigated in recent theoretical work.^{5,6,12,13} This consideration is based on recent experimental results of atomic mobilities on surface. E.g., the activation energy of step mobility for Ge on Ge(001) surface was measured to be smaller than that of Si on Si(001),⁴² corresponding to much larger atomic mobility for Ge. However, during the MBE growth for semiconductors (e.g., Si-Ge system or III-V alloys), dimerized atoms are quickly formed on (001) top surface when new materials are deposited, leading to a typical phenomenon of surface reconstruction.⁴³ These dimers, which may be comprised of unlike alloy components or like atoms, diffuse over the surface with diffusion processes and properties more complicated than and different from that of monomers.⁴⁴ For example, in Ge-on-Si submonolayer system the surface pattern with Si-Ge mixed dimers rather than Ge-Ge dimers can be observed.⁴⁵ A mixed Si-Ge dimer can diffuse as a unit, or transform into a pure dimer between like atoms (Si-Si) due to atomic exchange with underlying substrate atom and can also return back to the mixed form due to re-exchange process.^{44,45} Therefore, different alloy components deposited on surface may or may not diffuse independently. In the following studies we consider an effective surface mobility (or effective surface diffusivity D_s) to describe the processes of surface diffusion and decomposition in continuum approximation.

In this paper our starting point is the work of Léonard and Desai. It is reviewed in Ref. 46 and the basic model on which some refinements are made is described in Ref. 20. Here we further develop the model to a more general case, and more importantly, we consider two key features in the epitaxial growth systems: The first one is the coupling between top surface and underlying bulk of the growing film, which leads to a new dynamic equation for the evolution of surface compositional variable (ϕ_s); the second one is the composition dependence of all the three elastic constants, including the Young's modulus E , shear modulus μ and Poisson ratio $\nu (= E/2\mu - 1)$. In Ref. 20, the shear modulus was assumed to be constant and the surface-bulk coupling was neglected in dynamical equations. These new considerations can lead to stability results different from that of the previous theoretical work for strained alloy films,^{8,9,10,12,13,14,18,20} and more complicated and richer properties of the system can be obtained. Here we are interested in the growing films with deposition rate $v \neq 0$, while the results for isothermal annealing alloy films without growth ($v = 0$) are presented elsewhere.⁴⁷ The details of our model for the growth of thin alloy films are described in Sec. II. In Sec. III we present the solution of mechanical equilibrium for the system (More general results for mechanical equilibrium solution are given in Appendix A). In Sec. IV we use the results of Sec. III to derive self-contained dynamic equations for morphological and compositional perturbations, which we then use to perform a linear stability analysis; this leads to the characteristic equation for perturbation growth rate. The formulae of elastic free energy in Fourier space, which are needed in the derivation of Sec. IV, are given in Appendix B. The results of stability analysis for both the composition independent and composition dependent elastic moduli, including the stability diagrams, are presented in Sec. V. The behavior of kinetic critical thickness is presented in Sec. VI. Finally we conclude with a summary of salient features of our results in Sec. VII.

II. MODEL

Let us consider a strained alloy system composed of a semi-infinite substrate occupying the region $z < \zeta(x, y)$ and a $A_{1-X}B_X$ binary or pseudo-binary alloy film in the region $\zeta(x, y) < z < h(x, y, t)$. Here $\zeta(x, y)$ refers to the vertical position at which the film-substrate interface is located, and $h(x, y, t)$ is the surface height variable of the growing film. Usually, $\zeta(x, y)$ is assumed to be constant, or for simplicity 0, corresponding to a planar film-substrate interface fixed at $z = 0$.⁴⁸ The local composition within the film can be denoted by a continuous variable $\phi(\mathbf{r}, t)$ which is proportional to the difference in the local concentrations of two alloy constituents. Its average value $\bar{\phi}$ is equal to $2X - 1$, with X the alloy composition. Here we focus on the symmetric mixture film, i.e., $X = 1/2$ alloy for which $\bar{\phi} = 0$, while in the substrate $z \leq \zeta$ we have $\phi = 0$ since the compositional fluctuation is usually assumed to be absent there.

For this system of epitaxial growth, the film is assumed to be elastically isotropic and coherent with the substrate, without any misfit dislocations or other defects. On the top surface of the growing film, the evaporation and recondensation are negligible if the deposition of material occurs under ultra-high vacuum condition, like the growth through MBE, and then the system evolution should correspond to conserved dynamics. We also assume that there is no interdiffusion between film and substrate, and the diffusion and compositional relaxation in the bulk film can be neglected, since the bulk mobility of film components is miniscule compared to that on the surface in typical epitaxial growth. The neglect of the bulk mobility implies that the composition profile within the film reflects the time-history of the growing film and is dependent on the deposition rate v . As well the layers within the film are buried metastable layers which are frozen on account of negligible mobility in the bulk. Therefore, the bulk concentration field ϕ_b at some time t is equal to the surface field ϕ_s of an earlier time, i.e., $\phi_b(x, y, z, t) = \phi_s(x, y, t - t_0)$ for $z < h$, where $t_0 \sim (\bar{h} - z)/v$ with $\bar{h} = vt$ the average surface height, and then we have

$$\phi_b(x, y, z, t) \sim \phi_s(x, y, t = z/v). \quad (1)$$

Consequently, the conserved dynamics of morphological and compositional evolution is dominated by the surface diffusion and surface decomposition processes, with two time-dependent essential dynamical variables: the surface morphology $h(x, y, t)$ and the concentration field at the surface $\phi(x, y, z = h(x, y, t), t) \equiv \phi_s(x, y, t)$. The evolution equation describing the time dependence of h is^{20,22}

$$\frac{\partial h}{\partial t} = \Gamma_h \sqrt{g} \nabla_s^2 \frac{\delta \mathcal{F}}{\delta h} + v, \quad (2)$$

where v represents the deposition rate or growth velocity, ∇_s^2 is the surface Laplacian, $g = 1 + |\nabla h|^2$ denotes the determinant of the surface metric, and $\Gamma_h = D_s N_s / k_B T N_v^2$ is the kinetic coefficient⁴⁹ which depends on the surface diffusivity D_s , the Boltzmann constant k_B , growth temperature T , as well as the number density of atoms per unit surface area N_s and that per unit volume N_v . For the concentration field ϕ , the conserved dynamics leads to

$$\frac{\partial \phi}{\partial t} = \Gamma_\phi \nabla^2 \frac{\delta \mathcal{F}}{\delta \phi} - \Lambda \phi \Delta(z - h), \quad (3)$$

where Λ is proportional to film deposition rate v , corresponding to the tendency of surface composition to go towards the homogeneous phase (of $X = 1/2$ and $\bar{\phi} = 0$ in this paper) driven by the uniform deposition flux of material,^{22,50} and $\Delta(z - h)$ is zero everywhere except on the top surface $z = h$, where it is 1. Here the mobility Γ_ϕ is approximately zero in bulk, while at surface it is $\Gamma_\phi = \Gamma_h \delta^{-1}$ with δ the effective diffusion thickness of surface layer. The total free energy functional \mathcal{F} in Eqs. (2) and (3) makes the evolution of variables h and ϕ coupled with each other and consists of three contributions:

$$\mathcal{F} = \mathcal{F}_s + \mathcal{F}_{\text{GL}} + \mathcal{F}_{\text{el}}, \quad (4)$$

with the surface energy \mathcal{F}_s , the Ginzburg-Landau free energy \mathcal{F}_{GL} , and the elastic energy \mathcal{F}_{el} . The addition of deposition noise and thermal noise terms in the dynamical equations for h and ϕ have been considered earlier.²² At the level of linear stability analysis, neglecting noise does not alter the results. In Eq. (3) there are two ways to evaluate the surface composition fluctuations. The first one²⁰ is only considering the surface state and surface free energy, that is, evaluating the free energy \mathcal{F} at surface $z = h$ and then calculating the functional differentiation directly with respect to surface composition field $\phi_s(x, y, t)$ to obtain its evolution behavior. In this paper, we also take into account the coupling between surface and underlying bulk of the growing film by (i) identifying the free energy \mathcal{F} as the total energy of the system, that is, from $z = -\infty$ to $z = h$, and not just the one evaluated at surface $z = h$, (ii) then calculating $\nabla^2 \delta \mathcal{F} / \delta \phi$ as a whole, and finally (iii) evaluating its value as well as the other terms in Eq. (3) at surface $z = h$ to obtain the dynamics of surface field ϕ_s . This is analogous in spirit to the procedure in the previous study of surface critical phenomena for spin fluctuations.⁵¹

The surface energy contribution \mathcal{F}_s to the free energy (4) plays a stabilizing role and can be represented by a drumhead model without pinning term:

$$\mathcal{F}_s[h] = \gamma \int d^2r \sqrt{g}, \quad (5)$$

where γ is the surface tension at the top surface assumed to be isotropic and composition independent.⁵² The alloy thermodynamics is enforced through the Ginzburg-Landau functional

$$\mathcal{F}_{\text{GL}}[\phi, h] = \int_{\zeta}^h d^3r \left[-\frac{r'}{2}\phi^2 + \frac{u}{4}\phi^4 + \frac{c}{2}|\nabla\phi|^2 \right], \quad (6)$$

where the coefficients can be expressed as $r' = k_B(T_c - T)N_v$ and $c = k_B T_c N_v \lambda_0^2/2$, with T_c the critical temperature of the binary alloy and λ_0 the interaction distance which is of the order of lattice spacing.⁵³ In the absence of elastic effect, when $T > T_c$ the equilibrium state of bulk alloy is homogeneous with $\phi = 0$, while for $T < T_c$ two phases $\phi = \pm\sqrt{r'/u}$ coexist in equilibrium. The gradient energy term in Eq. (6) is important for stability analysis. It penalizes the sharp compositional changes and without this term a nonphysical divergence for short wavelength mode will occur.^{9,11,12} The coefficient c of this gradient energy term is related to the interfacial tension arising at the interface between coexisting phases.

The elastic free energy functional \mathcal{F}_{el} is important in any stress-driven system such as a growing film. Linear elasticity theory provides its expression as

$$\mathcal{F}_{\text{el}}[\phi, \mathbf{u}, h] = \frac{1}{2} \int_{-\infty}^h d^3r S_{ijkl} \sigma_{ij} \sigma_{kl}, \quad (7)$$

where σ_{ij} is the stress tensor and S_{ijkl} is the elastic compliance tensor with subscripts i, j, k , or $l = x, y, z$. For the isotropic system assumed here, we have $S_{ijkl} = \delta_{ik}\delta_{jl}(1 + \nu)/E - \delta_{ij}\delta_{kl}\nu/E$, with Young's modulus E and Poisson ratio ν . Generally, the elastic constants of the film depend on the local composition. In the first order approximation they are

$$\begin{aligned} E^f &= E_0^f(1 + E_1^*\phi), \\ \mu^f &= \mu_0^f(1 + \mu_1^*\phi), \end{aligned} \quad (8)$$

and $\nu^f = E^f/2\mu^f - 1$ (with μ the shear modulus), and the composition-independent results can be obtained by setting $E_1^* = \mu_1^* = 0$. In this paper, superscript f or s refers to the film or substrate respectively, and in most of our calculations below (except Appendix A) we neglect the difference between the average elastic constants of the film (E_0^f, μ_0^f , and $\nu_0^f = E_0^f/2\mu_0^f - 1$) and of the substrate (E^s, μ^s , and ν^s). This corresponds to the material systems with substrate and film having similar elastic constants.

Using the model developed here and the equations (2)–(8), we can explore the stability of the growing symmetric alloy films in the parameter space of lattice mismatch ϵ , solute expansion coefficient η , deposition rate v , growth temperature T , and the composition dependent elastic moduli parameters E_1^* and μ_1^* .

III. SOLUTION OF MECHANICAL EQUILIBRIUM

Thermodynamic equilibrium consists of mechanical, thermal and chemical equilibria. In the nonequilibrium system of growing alloy films that we are considering, the mechanical equilibrium occurs on a very fast time scale and we can assume that it occurs instantaneously. Thus by solving the equations of mechanical equilibrium, we can obtain the elastic displacement field \mathbf{u} in terms of the other two fields ϕ and h . This is the goal of this section. Knowing this solution, its substitution in the elastic free energy functional \mathcal{F}_{el} renders it dependent only on ϕ and h . The resulting effective elastic free energy functional is then used in the dynamic equations (2) and (3) for further analysis.

Inside both the film and substrate, the mechanical equilibrium yields

$$\partial_j \sigma_{ij} = 0, \quad (9)$$

where the linear elastic stress tensor σ_{ij} obeys the Hooke's law, and for the isotropic system studied here it is given by

$$\sigma_{ij}^f = 2\mu^f \left[\frac{\nu^f}{1 - 2\nu^f} u_{ll}^f \delta_{ij} + u_{ij}^f - \frac{1 + \nu^f}{1 - 2\nu^f} (\epsilon + \eta\phi) \delta_{ij} \right] \quad (10)$$

in the film, subjected to both the misfit strain ϵ and compositional strain $\eta\phi$, as well as

$$\sigma_{ij}^s = 2\mu^s \left[\frac{\nu^s}{1 - 2\nu^s} u_{ii}^s \delta_{ij} + u_{ij}^s \right] \quad (11)$$

in the substrate. Here $u_{ij} = (\partial_i u_j + \partial_j u_i)/2$ is the linear elastic strain tensor, and the reference state we use is the unconstrained state of substrate bulk lattice.

Considering the negligible external pressure on top surface of the film and the continuity of displacement and stress at the coherent film-substrate interface, we have the corresponding boundary conditions:

$$\sigma_{ij}^f n_j^f = 0 \quad \text{at} \quad z = h(x, y, t), \quad (12)$$

with n_j^f the unit vector normal to the surface, and

$$\sigma_{ij}^f n_j = \sigma_{ij}^s n_j \quad \text{and} \quad u_i^f = u_i^s \quad \text{at} \quad z = \zeta(x, y), \quad (13)$$

where n_j is the unit normal to the film-substrate interface and oriented toward the film. Moreover, in the substrate the displacement and strain are expected to vanish far from the interface, *i.e.*

$$u_i^s \rightarrow 0 \quad \text{and} \quad u_{ij}^s \rightarrow 0 \quad \text{for} \quad z \rightarrow -\infty. \quad (14)$$

To solve the above mechanical equilibrium equation, all the variables are expanded in Fourier series with a general form

$$\xi = \bar{\xi} + \sum_{\mathbf{q}} \hat{\xi}(\mathbf{q}, z, t) e^{i(q_x x + q_y y)}, \quad (15)$$

where ξ could represent different variables such as ϕ , h , u_i , and ζ , and $\hat{\xi}(\mathbf{q}, z, t)$ denotes the small perturbation around the basic state solution $\bar{\xi}$ (for height variable h or interface variable ζ , the perturbation should be expressed as $\hat{h}(\mathbf{q}, t)$ or $\hat{\zeta}(\mathbf{q})$, respectively). In the basic state, we have a uniform growing film with homogeneous composition $\bar{\phi} = 0$ and a planar front moving at constant rate v , corresponding to film thickness $\bar{h} = vt$. Due to the coherency of the film, the in-plane film lattice constant is equal to a^s and then $\bar{u}_x^f = \bar{u}_y^f = 0$. The Poisson relaxation in the z direction results in $\bar{u}_z^f = \bar{u}_{zz}^f z$, with $\bar{u}_{zz}^f = \bar{u} = \epsilon(1 + \nu_0^f)/(1 - \nu_0^f)$. The film is stressed in the lateral directions, leading to $\bar{\sigma}_{xx}^f = \bar{\sigma}_{yy}^f = \bar{\sigma} = -2\mu_0^f \bar{u}$, and all the other strains and stresses are zero. In the substrate, we have $\bar{u}_i^s = 0$ and $\bar{u}_{ij}^s = \bar{\sigma}_{ij}^s = 0$ for $i, j = x, y, z$, corresponding to an unstrained basic state.

The expansion forms of both the mechanical equilibrium (9) and boundary conditions (12)–(14) can be obtained using Eq. (15). Generally, due to composition dependence of film elastic constants, as depicted in Eq. (8), from Eqs. (9) and (10) one can obtain the extra terms proportional to coefficients E_1^* and μ_1^* in the mechanical equilibrium equation of the film, which is different from the composition independent case and more complicated (since the elastic constants also vary with position \mathbf{r} according to Eq. (8)). Here we only consider the solution of mechanical equilibrium to zeroth order of elastic moduli E^f and μ^f , which is applicable when E_1^* and μ_1^* are small enough, or E^f and μ^f are assumed to vary very slowly with space and the equation is considered to first order. Consequently, we obtain the mechanical equilibrium equation with a linear form as used before²⁰, but with different linearized boundary conditions due to the film-substrate interface roughness $\hat{\zeta}$. At the top surface of the film, *i.e.* $z = \bar{h}$, from Eq. (12) we have

$$\begin{aligned} \hat{\sigma}_{xz}^f &= iq_x \bar{\sigma} \hat{h}, \\ \hat{\sigma}_{yz}^f &= iq_y \bar{\sigma} \hat{h}, \\ \hat{\sigma}_{zz}^f &= 0, \end{aligned} \quad (16)$$

as before, while at interface $z = \bar{\zeta} = 0$, we have different conditions due to Eq. (13):

$$\begin{aligned} -iq_x \bar{\sigma} \hat{\zeta} + \hat{\sigma}_{xz}^f &= \hat{\sigma}_{xz}^s, \\ -iq_y \bar{\sigma} \hat{\zeta} + \hat{\sigma}_{yz}^f &= \hat{\sigma}_{yz}^s, \\ \hat{\sigma}_{zz}^f &= \hat{\sigma}_{zz}^s, \end{aligned} \quad (17)$$

and

$$\begin{aligned} \hat{u}_i^f &= \hat{u}_i^s \quad \text{for} \quad i = x, y, \\ \bar{u} \hat{\zeta} + \hat{u}_z^f &= \hat{u}_z^s. \end{aligned} \quad (18)$$

Finally, for $z \rightarrow -\infty$ condition (14) leads to

$$\hat{u}_i^s \rightarrow 0 \quad \text{and} \quad \partial_z \hat{u}_i^s \rightarrow 0. \quad (19)$$

The corresponding results of the solution for non-planar interface $\zeta \neq 0$ and differing film-substrate elastic constants are detailed in Appendix A. In the following studies for elastic free energy and dynamical equations, we assume a planar film-substrate interface,⁴⁸ *i.e.* $\zeta = 0$, as well as the equal average elastic constants between film and substrate, that is, $E_0^f = E^s = E_0$, $\mu_0^f = \mu^s = \mu_0$, and $\nu_0^f = \nu^s = \nu_0$. Thus, substituting these conditions in the results of Appendix A, one can obtain the solution

$$\hat{u}_i^f = \begin{bmatrix} \alpha_x \\ \alpha_y \\ \alpha_z \end{bmatrix} e^{qz} - \begin{bmatrix} iq_x/q \\ iq_y/q \\ 1 \end{bmatrix} C z e^{qz} + \left(\frac{1+\nu_0}{1-\nu_0} \right) \eta \begin{bmatrix} iq_x \hat{W} \\ iq_y \hat{W} \\ \partial_z \hat{W} \end{bmatrix}, \quad (20)$$

for the film, where $q^2 = q_x^2 + q_y^2$, and the coefficients α_i and C are given by

$$iq_x \alpha_x + iq_y \alpha_y = e^{-q\bar{h}} \left[(2(1-\nu_0) - q\bar{h}) \left(q\bar{u}\hat{h} + \left(\frac{1+\nu_0}{1-\nu_0} \right) \eta q \left(\partial_z \hat{W} \right)_{z=\bar{h}} \right) \right. \\ \left. + (-1 + 2\nu_0 + q\bar{h}) \left(\frac{1+\nu_0}{1-\nu_0} \right) \eta \left(\partial_z^2 \hat{W} - \hat{\phi} \right)_{z=\bar{h}} \right], \quad (21)$$

$$q\alpha_z = e^{-q\bar{h}} \left[(1 - 2\nu_0 + q\bar{h}) \left(q\bar{u}\hat{h} + \left(\frac{1+\nu_0}{1-\nu_0} \right) \eta q \left(\partial_z \hat{W} \right)_{z=\bar{h}} \right) \right. \\ \left. - (2(1-\nu_0) + q\bar{h}) \left(\frac{1+\nu_0}{1-\nu_0} \right) \eta \left(\partial_z^2 \hat{W} - \hat{\phi} \right)_{z=\bar{h}} \right], \quad (22)$$

$$C = e^{-q\bar{h}} \left[q\bar{u}\hat{h} + \left(\frac{1+\nu_0}{1-\nu_0} \right) \eta \left(q\partial_z \hat{W} - \partial_z^2 \hat{W} + \hat{\phi} \right)_{z=\bar{h}} \right], \quad (23)$$

with $q_y \alpha_x = q_x \alpha_y$. Here \hat{W} is introduced through the particular solution of the mechanical equilibrium equation, as shown in the last term of Eq. (20), and is defined through

$$(\partial_z^2 - q^2) \hat{W} = \hat{\phi}, \quad (24)$$

or the relation $\nabla^2 W = \phi$ in real space.²⁰ Consequently, the results for strain and stress tensors can be obtained through e.g., Eq. (A6).

IV. DYNAMIC EQUATIONS AND PERTURBATION GROWTH RATE

To evaluate the dynamic equations (2) and (3) and then determine the evolution behaviors of surface profile, we should first calculate the total free energy \mathcal{F} . The first two contributions, surface and Ginzburg-Landau free energy, are given in Eqs. (5) and (6) explicitly, while the film elastic energy can be obtained from Eqs. (7) and (10):

$$\mathcal{F}_{\text{el}}^f = \int_0^h d^3r \left[\frac{1}{2} \lambda^f u_{ll}^{f2} + \mu^f u_{ij}^{f2} \right. \\ \left. + \frac{E^f}{1-2\nu^f} \left(\frac{3}{2} \epsilon^2 - \epsilon u_{ll}^f + 3\epsilon\eta\phi + \frac{3}{2} \eta^2 \phi^2 - \eta\phi u_{ll}^f \right) \right], \quad (25)$$

with the Lamé coefficient $\lambda^f = 2\mu^f\nu^f/(1-2\nu^f)$. In Eq. (25), the first two terms represent the general form of the isotropic elastic energy density for single-component system, and by setting $\epsilon = 0$ and renormalizing the Ginzburg-Landau free energy, which absorbs the ϕ^2 term, we can obtain the bulk elastic energy functional with the effect of compositional strain (*i.e.* coupling term $\eta\phi u_{ll}^f$) that has been widely used.^{21,54} Considering the composition

dependence of both Young's and shear moduli, we can write Eq. (25) to first order of E_1^* and μ_1^* as

$$\begin{aligned} \mathcal{F}_{\text{el}}^f = \int_0^h d^3r \left\{ \frac{1}{2} \lambda_0 u_{ll}^{f^2} + \mu_0 u_{ij}^{f^2} + \mu_0 \mu_1^* \phi u_{ij}^{f^2} \right. \\ + \frac{E_0}{1-2\nu_0} \left[\frac{3}{2} \epsilon^2 - \epsilon u_{ll}^f + 3 \left(\epsilon \eta + \frac{3E_1^* - 2(1+\nu_0)\mu_1^*}{2(1-2\nu_0)} \epsilon^2 \right) \phi \right. \\ + 3 \left(\frac{1}{2} \eta^2 + \frac{3E_1^* - 2(1+\nu_0)\mu_1^*}{1-2\nu_0} \epsilon \eta \right) \phi^2 - \left(\eta + \frac{3E_1^* - 2(1+\nu_0)\mu_1^*}{1-2\nu_0} \epsilon \right) \phi u_{ll}^f \\ + \frac{1}{2(1-2\nu_0)} \left(E_1^* - \frac{1+2\nu_0^2}{1+\nu_0} \mu_1^* \right) \phi u_{ll}^{f^2} - \frac{3E_1^* - 2(1+\nu_0)\mu_1^*}{1-2\nu_0} \eta \phi^2 u_{ll}^f \\ \left. \left. + \frac{3}{2} \left(\frac{3E_1^* - 2(1+\nu_0)\mu_1^*}{1-2\nu_0} \right) \eta^2 \phi^3 \right] \right\} \end{aligned} \quad (26)$$

with $\lambda_0 = 2\mu_0\nu_0/(1-2\nu_0)$. The corresponding Fourier expansion to second order of perturbation is given in Appendix B.

The strain tensor u_{ij}^f in elastic energy expression (26) can be determined from the solution of mechanical equilibrium shown in Eqs. (20)–(23) or Appendix A, and is in fact composed of two parts:

$$u_{ij}^f = u_{ij}^{\text{hom}} + u_{ij}^{\text{par}}. \quad (27)$$

The first part is the homogeneous solution and can be calculated through the first two terms of the displacement solution (20). The second part corresponds to the particular solution and is given by

$$u_{ij}^{\text{par}} = \frac{1+\nu_0}{1-\nu_0} \eta \partial_i \partial_j W. \quad (28)$$

Note that the homogeneous part u_{ij}^{hom} is in fact not the function of system variable ϕ or W , and the coefficients in this part, α_i and C in Eqs. (21)–(23), depend on $(\partial_z \hat{W})_{z=\bar{h}}$, $(\partial_z^2 \hat{W})_{z=\bar{h}}$, and $\hat{\phi}|_{z=\bar{h}}$ which are surface values (of fixed z for certain time t) evaluated at $z = \bar{h}$ due to the boundary condition at top surface. Therefore, when performing the functional differentiation of the free energy with respect to system variable ϕ , only the particular solution (28) of strain tensor needs to be considered.⁵⁵

The dynamical equation for compositional perturbation at the surface can be determined by substituting energy formulae (5), (6) and (26) into Eq. (3). When expanded to first order, it is

$$\partial \hat{\phi}_s / \partial t = -\Gamma_\phi q^2 (-r' + cq^2) \hat{\phi}_s + \Gamma_\phi \left(\nabla^2 \frac{\delta \mathcal{F}_{\text{el}}^f}{\delta \phi} \right) \bigg|_q \bigg|_s - \Lambda \hat{\phi}_s, \quad (29)$$

with the elastic energy term $(\nabla^2 \delta \mathcal{F}_{\text{el}}^f / \delta \phi)_q|_s$ obtained from the Fourier expansion using Eq. (26):

$$\begin{aligned} \left(\nabla^2 \frac{\delta \mathcal{F}_{\text{el}}^f}{\delta \phi} \right) \bigg|_q \bigg|_s = -q^2 \left\{ \left[\frac{E_0(3-\nu_0)}{(1-\nu_0)^2} \eta^2 + \frac{E_0(2(5-7\nu_0)E_1^* - (7-10\nu_0)(1+\nu_0)\mu_1^*)}{(1-\nu_0)^2(1-2\nu_0)} \epsilon \eta \right] \hat{\phi}_s \right. \\ \left. - \left[\frac{E_0}{1-\nu_0} \eta + \frac{E_0(2E_1^* - (1+2\nu_0)\mu_1^*)}{(1-2\nu_0)(1-\nu_0)} \epsilon \right] \hat{u}_{ll}^f|_s + \frac{E_0}{1-\nu_0} \mu_1^* \epsilon \hat{u}_{zz}^f|_s \right\}, \end{aligned} \quad (30)$$

where we have used the continuity condition of $\nabla^2 \phi$ at surface: $(\nabla^2 \phi)_s = \nabla_s^2 \phi_s$, which implies that $[(\partial_z^2 \phi)_s]_q \approx 0$ since we ignore terms of order $\hat{h}^2 \hat{\phi}_s$.

For the evolution of surface height variable h , we can obtain the following linearized dynamical equation by combining Eq. (2) and the free energy functionals (5), (6) and (26):

$$\partial \hat{h} / \partial t = -\Gamma_h q^2 \left(\gamma q^2 \hat{h} + \hat{\mathcal{E}}^f|_s \right), \quad (31)$$

where $\hat{\mathcal{E}}^f|_s$ is the first order elastic free energy density evaluated at the surface, with the expression given in Eq. (B3) of Appendix B.

Since what we are interested in is the stability property of this growing alloy system with respect to small perturbations, we focus on the film behavior of the early evolution time regime, where the morphological and compositional perturbations at the surface are assumed to evolve exponentially:

$$\hat{h} = \hat{h}_0(q)e^{\Omega_h t} \quad \text{and} \quad \hat{\phi}_s = \hat{\phi}_0(q)e^{\Omega_\phi t}, \quad (32)$$

with Ω_h and Ω_ϕ the growth rates of surface perturbations for h and ϕ , respectively. Due to the coupling of dynamical equations (2) and (3) in general case, the joint stability or instability, corresponding to $\Omega_h = \Omega_\phi = \Omega$, is obtained. Considering the expression (1) for bulk composition field, we have²⁰ $\hat{\phi} = \hat{\phi}_0 \exp(\Omega z/v)$, and then $\hat{W} = v^2 \hat{\phi}/(\Omega^2 - q^2 v^2)$ from Eq. (24). Consequently, by substituting this approximate form of \hat{W} into the solution for film displacement vector \hat{u}_i^f (20)–(23), we can calculate formula (30) as well as the linear elastic energy density $\hat{\mathcal{E}}^f|_s$ in term of two surface fields \hat{h} and $\hat{\phi}_s$, as shown in Appendix B.

For further analysis, it is convenient to introduce a characteristic length scale representing the typical size of interfaces between surface domains:

$$l_0 = \left(\frac{|r|}{c} \right)^{-1/2}, \quad (33)$$

as well as a diffusive time scale

$$\tau_0 = \left(\Gamma_\phi \frac{r^2}{c} \right)^{-1}, \quad (34)$$

where $r = r' - 2E_0\eta^2/(1 - \nu_0) = k_B(T_c^{\text{eff}} - T)N_v$ is a renormalized coefficient with the effective critical temperature

$$T_c^{\text{eff}} = T_c - \frac{2E_0}{1 - \nu_0} \frac{\eta^2}{k_B N_v}. \quad (35)$$

Note that T_c^{eff} used here is just the bulk coherent spinodal temperature derived by Cahn⁴ for binary stressed alloys. Using the following transformations

$$\begin{aligned} k &= ql_0, \\ \tau &= t/\tau_0, \\ V &= v\tau_0/l_0 = \Lambda\tau_0, \\ \sigma &= \Omega\tau_0, \\ \gamma^* &= \gamma l_0/c, \\ \epsilon^* &= \left[\frac{2E_0}{|r|} \left(\frac{1 + \nu_0}{1 - \nu_0} \right) \right]^{1/2} \epsilon, \\ \eta^* &= \left[\frac{2E_0}{|r|} \left(\frac{1 + \nu_0}{1 - \nu_0} \right) \right]^{1/2} \eta, \end{aligned} \quad (36)$$

where we have set $\Gamma_h/\Gamma_\phi = \delta = l_0$, as well as

$$\begin{aligned} \hat{h}^* &= h/l_0, \\ \hat{\phi}_s^* &= \hat{\phi}_s, \end{aligned} \quad (37)$$

we reduce the dynamical equations (31) and (29) for surface perturbations to dimensionless forms:

$$\partial \hat{h}^* / \partial \tau = (\epsilon^{*2} k^3 - \gamma^* k^4) \hat{h}^* - \frac{k^2}{1 + \nu_0} \left[\epsilon^* \eta^* \left(\frac{\sigma - kV\nu_0}{\sigma + kV} \right) + \frac{2E_1^* - (1 + \nu_0)\mu_1^*}{2(1 - \nu_0)} \epsilon^{*2} \right] \hat{\phi}_s^*, \quad (38)$$

and

$$\begin{aligned} \partial \hat{\phi}_s^* / \partial \tau &= \frac{k^3}{1 - \nu_0} \left[(1 - 2\nu_0) \epsilon^* \eta^* + (2E_1^* - (1 + \nu_0)\mu_1^*) \epsilon^{*2} \right] \hat{h}^* \\ &+ \left[-k^2 \left(k^2 \pm 1 + \frac{8E_1^* - 5(1 + \nu_0)\mu_1^*}{2(1 - \nu_0^2)} \epsilon^* \eta^* \right) - V \right. \\ &\left. + \frac{1}{1 - \nu_0} \left((1 - 2\nu_0) \eta^{*2} + (2E_1^* - (1 + \nu_0)\mu_1^*) \epsilon^* \eta^* \right) \frac{k^3 V}{\sigma + kV} \right] \hat{\phi}_s^*, \end{aligned} \quad (39)$$

where for sign “ \pm ”, the top sign applies when the system is above the effective critical temperature T_c^{eff} and the bottom sign is taken if $T < T_c^{\text{eff}}$.

Due to the rescaling (36), the early time behavior of perturbations (32) is transformed to $\hat{h}^* = \hat{h}_0^* \exp(\sigma_h \tau)$ and $\hat{\phi}_s^* = \hat{\phi}_0^* \exp(\sigma_\phi \tau)$ with the nondimensional perturbation growth rates σ_h and σ_ϕ . Generally, the dynamical equations (38) and (39) for \hat{h}^* and $\hat{\phi}_s^*$ couple with each other, resulting in a cubic characteristic equation for perturbation growth rate $\sigma_h = \sigma_\phi = \sigma$:

$$\begin{aligned} & (\sigma + \gamma^* k^4 - \epsilon^{*2} k^3) \left[\sigma + k^2 \left(k^2 \pm 1 + \frac{8E_1^* - 5(1 + \nu_0)\mu_1^*}{2(1 - \nu_0^2)} \epsilon^* \eta^* \right) \right. \\ & \quad \left. - \frac{1}{1 - \nu_0} \left((1 - 2\nu_0)\eta^{*2} + (2E_1^* - (1 + \nu_0)\mu_1^*)\epsilon^* \eta^* \right) \frac{k^3 V}{\sigma + kV} + V \right] \\ & + \frac{k^5}{1 - \nu_0^2} \left[(1 - 2\nu_0)\epsilon^* \eta^* + (2E_1^* - (1 + \nu_0)\mu_1^*)\epsilon^{*2} \right] \\ & \times \left[\epsilon^* \eta^* \left(\frac{\sigma - kV\nu_0}{\sigma + kV} \right) + \frac{2E_1^* - (1 + \nu_0)\mu_1^*}{2(1 - \nu_0)} \epsilon^{*2} \right] = 0. \end{aligned} \quad (40)$$

When the real part of σ is larger than zero, the initial perturbations will grow with time, leading to the instability of the growing film; otherwise the surface perturbations will decay in time, making the system stable. Note that this characteristic equation (40) is asymmetric with respect to the sign of rescaled misfit ϵ^* , leading to the asymmetry of stability properties between compressive and tensile films as specified below, but it is symmetric for $(\epsilon^*, \eta^*) \rightarrow (-\epsilon^*, -\eta^*)$, similar to the previous results.^{9,12} Thus, in the following analysis we keep $\eta^* \geq 0$ and consider different signs of ϵ^* .

Setting $E_1^* = \mu_1^* = 0$ in above deductions we can obtain the corresponding results for system with composition independent elastic constants. The corresponding equation for \hat{h}^* is the same as that for \hat{h}^* in Ref. 20, but the equations for $\hat{\phi}_s^*$ are quite different due to the fact that here we consider the total energy of the film and the surface-bulk coupling, while in Ref. 20 only the surface energy is used (see also Appendix B). Consequently, the characteristic equations for σ are also different, and our Eq. (40) reduces to a cubic, which is also different from that of the previous related work carried out by Guyer and Voorhees^{8,9,10,11} and Spencer *et al.*^{12,13,14} due to different models and approximations. Compared with Eq. (40), this cubic equation shows the symmetry with respect to the sign of ϵ^* for systems with composition independent elastic moduli.

V. STABILITY DIAGRAMS

The typical dispersion relations of $\text{Re}(\sigma)$, which is the real part of joint perturbation growth rate σ , as a function of rescaled wavenumber k are depicted in Fig. 1 for systems with composition dependent elastic moduli and $T > T_c^{\text{eff}}$. The value of $\text{Re}(\sigma)$ in Fig. 1 for each k is in fact defined as the largest real part of the three solutions of characteristic equation (40), since that will be the dominant growth in case of instability. Note that for very large k values we always have $\text{Re}(\sigma) \rightarrow -\infty$, even when η^* is large, corresponding to short wavelength stabilization. This is different from the previous work^{9,11,12} where nonphysical divergence for $k \rightarrow \infty$ and large η^* occurs due to the absence of gradient term in free energy functional. If $\text{Re}(\sigma)$ is smaller than zero for all k , e.g., the dashed curve in Fig. 1, the system is stable; otherwise, we can find a band of wavenumbers for which the surface profiles are unstable to fluctuations. In the following we investigate the stability properties and the effects of misfit strain, compositional stress, deposition rate, as well as the composition dependence of elastic constants more systematically, by determining the maximum of $\text{Re}(\sigma)$ with respect to all disturbance modes k for different material parameters.

A. Analytic results for special cases

We first consider some simple cases where the misfit strain or solute stress is absent and then the analytic results can be available. The simplest case corresponds to $\epsilon^* = \eta^* = 0$, *i.e.* a lattice-matched film with constituents having the same size, for which dynamical equations (38) and (39) decouple, resulting in different perturbation growth rates for \hat{h}^* and $\hat{\phi}_s^*$, as found in previous work:²⁰

$$\sigma_h = -\gamma^* k^4, \quad (41)$$

$$\sigma_\phi = -k^4 \mp k^2 - V. \quad (42)$$

Formula (41) implies the stability of film morphology since σ_h is always negative. Eq. (42) yields the stable compositional profile for $T > T_c^{\text{eff}}$ (top sign “-”), whereas for $T < T_c^{\text{eff}}$ the competition between the deposition of homogeneous materials and surface decomposition leads to a critical deposition rate $V_c = 1/4$. When $V > V_c$ the film is stable with respect to compositional fluctuations, otherwise phase separation occurs.

When misfit strain exists ($\epsilon^* \neq 0$) but solute stress is absent ($\eta^* = 0$), we have different results for systems with composition independent and composition dependent elastic moduli. When $E_1^* = \mu_1^* = 0$, the height variable and composition field still decouple, and we can recover the result of Asaro and Tiller¹ and Grinfeld² for morphological instability, which is

$$\sigma_h = \epsilon^{*2} k^3 - \gamma^* k^4. \quad (43)$$

The stability of compositional perturbation is also governed by Eq. (42), in accord with the previous result.²⁰ However, when the elastic constants are dependent on film composition, $E_1^* \neq 0$ and $\mu_1^* \neq 0$ make the dynamical equations for \hat{h}^* and ϕ_s^* coupled, and then the joint perturbation growth rate $\sigma_h = \sigma_\phi = \sigma$ obeys a quadratic equation

$$\sigma^2 + a_1 \sigma + a_0 = 0, \quad (44)$$

with coefficients

$$\begin{aligned} a_1 &= \gamma^* k^4 - \epsilon^{*2} k^3 + k^2(k^2 \pm 1) + V, \\ a_0 &= (\gamma^* k^4 - \epsilon^{*2} k^3)[k^2(k^2 \pm 1) + V] + \frac{[2E_1^* - (1 + \nu_0)\mu_1^*]^2}{2(1 + \nu_0)(1 - \nu_0)^2} \epsilon^{*4} k^5. \end{aligned} \quad (45)$$

Note that the solution form for quadratic (44) is $\sigma = (-a_1 \pm \sqrt{a_1^2 - 4a_0})/2$, and we have maximum $\text{Re}(\sigma) > 0$ due to $a_1 > 0$ and $a_0 < 0$ obtained from (45) when $k \ll 1$, for both T above and below T_c^{eff} . Therefore, for the lattice mismatched film without solute stress, the morphological profile and compositional mode couple with each other if we consider the composition dependence of elastic moduli, and then the misfit strain can not only cause the morphological instability, but also the phase separation in spite of uniform deposition, which is different from the previous stability results.^{14,20}

So far in this subsection, we have considered different cases all of which have $\eta^* = 0$. From Eq. (35), we note that for these cases T_c^{eff} is same as T_c .

The case for no misfit strain ($\epsilon^* = 0$) but nonzero solute stress ($\eta^* \neq 0$) can determine the role of compositional strain on film stability (without the interplay with misfit). The same results of perturbation rate can be obtained from dynamical equations for composition dependent (Eqs. (38) and (39)) and composition independent elastic moduli. That is, the morphological and compositional modes decouple, with σ_h given by Eq. (41), resulting in stable morphology of this lattice-matched film. The property of compositional perturbation is more complicated, with σ_ϕ governed by a quadratic similar to (44):

$$\sigma_\phi^2 + a_1 \sigma_\phi + a_0 = 0,$$

where the coefficients are

$$\begin{aligned} a_1 &= k^2(k^2 \pm 1) + (k + 1)V, \\ a_0 &= kV \left[k^2(k^2 \pm 1) - k^2 \left(\frac{1 - 2\nu_0}{1 - \nu_0} \right) \eta^{*2} + V \right]. \end{aligned} \quad (46)$$

The stability conditions for compositional profile can then be calculated analytically through the solutions of this quadratic equation for σ_ϕ . For growth temperature T higher than bulk coherent spinodal T_c^{eff} , which corresponds to the case of most experiments, phase separation can occur only when η^* is larger than a critical value η_c^* , while for $\eta^* < \eta_c^*$ the lattice-matched alloy film is stable against decomposition. Different condition applies to low temperature $T < T_c^{\text{eff}}$, for which there is no critical value like η_c^* for the appearance of alloy decomposition, and larger deposition rate V can suppress the instability. In more detail, the *stability* condition for $T > T_c^{\text{eff}}$ is given as

$$\begin{aligned} \eta^{*2} &< \eta_c^{*2} = \frac{1 - \nu_0}{1 - 2\nu_0} \quad \text{for any } V \\ \text{or} \\ \eta^{*2} &> \eta_c^{*2} \quad \text{and} \quad V > \frac{1}{4} \left[1 - (\eta^*/\eta_c^*)^2 \right]^2. \end{aligned} \quad (47)$$

For $T < T_c^{\text{eff}}$ the compositional profile is stabilized with the condition of high deposition rate

$$V > \frac{1}{4} \left[1 + (\eta^*/\eta_c^*)^2 \right]^2, \quad (48)$$

which is fulfilled for any η^* , with the value of η_c^* given in Eq. (47). The corresponding stability diagrams calculated from Eqs. (47) and (48) are plotted in Fig. 2, with $\nu_0 = 1/4$ for which $\eta_c^{*2} = 1.5$. In both Fig. 2 (a) and Fig. 2 (b), the compositional profile is stable in the region of high deposition rate $V > V_c$, with V_c generally increasing with the value of η^* except for a special region of $T > T_c^{\text{eff}}$. This special region corresponds to $\eta^* < \eta_c^*$ as given in Eq. (47), and in this range of η^* we have $V_c = 0$, that is, the system is always stable.

Therefore, our results for this instability driven by compositional stress, in the absence of misfit, are different from those of earlier works,^{11,12} where the compositional instability is expected only below an effective temperature which increases with η^2 , but is higher than the coherent spinodal T_c^{eff} used here and independent of deposition rate V . Our calculations exhibit more complicated behavior, that is, the solute stress enhances the compositional modulation only when exceeding a critical value (η_c^*) for $T > T_c^{\text{eff}}$, and this stress driven instability can be suppressed by large deposition rate, as illustrated in Fig. 2 as well as Eqs. (47) and (48). Note that both the increase form of V_c and the value of η_c^* in Fig. 2 are different from that of Ref. 20, due to different models and characteristic equations for σ_ϕ .

B. Stability diagrams in general case

Generally, both misfit strain and solute stress are nonzero in strained alloy film growth, corresponding to $\epsilon^* \neq 0$, $\eta^* \neq 0$, and the coupling of dynamical equations for surface height and compositional variables. Thus, the growth of morphological disturbance will induce the decomposition and phase separation of alloy film, and vice versa, resulting in the simultaneous occurrence of stability or instability for morphological and compositional profiles. The joint perturbation growth rate is then determined by the cubic characteristic equation (40), which can be rewritten as

$$\sigma^3 + a_2\sigma^2 + a_1\sigma + a_0 = 0, \quad (49)$$

with the three coefficients:

$$\begin{aligned} a_2 &= \gamma^* k^4 - \epsilon^{*2} k^3 + k^2 (k^2 \pm 1 + \beta_0 \epsilon^* \eta^*) + (k+1)V, \\ a_1 &= (\gamma^* k^4 - \epsilon^{*2} k^3 + kV) [k^2 (k^2 \pm 1 + \beta_0 \epsilon^* \eta^*) + V] \\ &\quad + kV (\gamma^* k^4 - \epsilon^{*2} k^3) - \frac{k^3 V}{1 - \nu_0} [(1 - 2\nu_0) \eta^{*2} + \alpha_0 \epsilon^* \eta^*] \\ &\quad + \frac{k^5}{2(1 + \nu_0)(1 - \nu_0)^2} [(1 - 2\nu_0) \epsilon^* \eta^* + \alpha_0 \epsilon^{*2}] [2(1 - \nu_0) \epsilon^* \eta^* + \alpha_0 \epsilon^{*2}], \\ a_0 &= (\gamma^* k^4 - \epsilon^{*2} k^3) \left\{ kV [k^2 (k^2 \pm 1 + \beta_0 \epsilon^* \eta^*) + V] - \frac{k^3 V}{1 - \nu_0} [(1 - 2\nu_0) \eta^{*2} + \alpha_0 \epsilon^* \eta^*] \right\} \\ &\quad + \frac{k^6 V}{2(1 + \nu_0)(1 - \nu_0)^2} [(1 - 2\nu_0) \epsilon^* \eta^* + \alpha_0 \epsilon^{*2}] [-2\nu_0(1 - \nu_0) \epsilon^* \eta^* + \alpha_0 \epsilon^{*2}]. \end{aligned} \quad (50)$$

Here the parameters α_0 and β_0 are defined as

$$\begin{aligned} \alpha_0 &= 2E_1^* - (1 + \nu_0)\mu_1^*, \\ \beta_0 &= \frac{8E_1^* - 5(1 + \nu_0)\mu_1^*}{2(1 - \nu_0^2)}. \end{aligned} \quad (51)$$

We can determine the stability properties with respect to different parameters such as ϵ^* , η^* , V , and T from the largest real-part root of above characteristic equations, which can be obtained from the dispersion relations similar to those shown in Fig. 1. In this and the following sections two sets of material parameters are used, corresponding to two typical types of stability properties. In the first set, we choose $\nu_0 = 1/4$, $\gamma^* = 5$, η^* around 0.6, as well as $E_1^* = -0.4$ and $\mu_1^* = -0.1$ if considering the composition dependent elastic moduli, which qualitatively represents the alloy films of SiGe type. The second set corresponds to the systems of pseudo-binary III-V alloys such as InGaAs, with the chosen parameters $\nu_0 = 1/3$, $\gamma^* = 3.5$, η^* around 1.1, and $E_1^* = -0.25$, $\mu_1^* = -0.5$ if applied. These parameter values have been arrived at by using the rescaling formulae (36) as well as different types of material parameters for group IV and III-V components presented in Ref. 8 (e.g., the elastic moduli and the atomic size difference for alloy

components that determines η). The parameters such as the elastic constants and lattice parameters are estimated from the average of the quantities for pure components (e.g., Si and Ge or InAs and GaAs), while E_1^* and μ_1^* are adjustable but should be qualitatively consistent with the variation trend of E and ν between pure alloy components.

In Figs. 3 and 4 we plot the stability diagrams of dimensionless deposition rate V versus misfit strain ϵ^* for different values of η^* , including different cases of growth temperatures (above or below coherent spinodal T_c^{eff}) and of composition dependence or independence of elastic moduli. When one compares Figs. 3 (a) and 4 (a), the stability diagrams are qualitatively similar. For $E_1^* = \mu_1^* = 0$, the stability boundaries are symmetric with respect to sign of ϵ^* and qualitatively insensitive to changes in ν_0 or γ^* . The major qualitative difference between these two figures is seen for the case of composition dependent elastic constants, *i.e.* when $E_1^* \neq 0$ and $\mu_1^* \neq 0$, as we compare Fig. 3 (b) with Fig. 4 (b) which are for $T > T_c^{\text{eff}}$. These stability results are clearly asymmetric with respect to the sign of misfit ϵ^* . Similar asymmetry also occurs for $T < T_c^{\text{eff}}$. This asymmetry emerges from the characteristic equation (40), and is enhanced by larger solute stresses (*i.e.* larger values of η^*). However, the form of asymmetry is dependent on the choice of parameters. In Fig. 3, the parameters of SiGe-type are used and the stability diagrams show that the instability region of a film under compressive strain ($\epsilon^* > 0$) is larger than that under tensile strain ($\epsilon^* < 0$), while in Fig. 4 with InGaAs-type parameters, we have opposite result that the compressive films have larger stability region. This asymmetry of stability has also been found in earlier works of Guyer and Voorhees^{8,9,10,11} and Leonard and Desai^{18,20} (for the case of composition dependent Young modulus) when single surface mobility is considered. However, in these results only one kind of asymmetry is obtained, that is, tensile films are more stable than compressive films, while our calculations yields different kinds of asymmetry due to different parameters E_1^* and μ_1^* determined by composition dependent behavior of elastic moduli. Note that most experiments are carried out at temperature $T > T_c^{\text{eff}}$, with growth parameters corresponding to very small rescaled deposition rate V and for rescaled η^* (~ 0.6 for SiGe film and ~ 1.1 for InGaAs growth) that is not large. Thus, to compare with available experimental observations, we should study the bottom part and the lowest curve of diagrams in Figs. 3 (b) and 4 (b), which, however, have very weak asymmetry. In the next section, we will present the results for kinetic critical thickness on the scales corresponding to experimental parameters, and the asymmetry of (effective) stability will be shown more clearly, with more complex behavior for InGaAs-type films.

A common feature of the diagrams in Figs. 3 and 4 is that the system can be completely stabilized by large enough deposition rate V , the value of which is determined by material parameters like ϵ^* and η^* . This stabilization effect at large deposition rate can be understood as follows. First, when the materials are deposited fast enough, the former surface layer is buried and then frozen (due to miniscule bulk mobility) before the surface morphological undulation and phase segregation have enough time to develop through surface diffusion. Second, as described in dynamical equation (3), the deposition flux is uniform and then have the tendency to drive the surface composition profile to the homogeneous phase of incident flux. Note that in Fig. 3 the scale of V in the stability diagrams ((c) and (d)) for $T < T_c^{\text{eff}}$ is much larger than those ((a) and (b)) for $T > T_c^{\text{eff}}$, due to the fact that in usual coherent systems, spinodal decomposition is apt to occur below the temperature T_c^{eff} , and then faster deposition is needed to suppress it. This effect of stabilization at high deposition rates has been found by Guyer and Voorhees^{9,10,11} and Leonard and Desai^{18,20}, but is absent in recent work of Spencer *et al.*^{12,14} for the case of equal mobilities of alloy components. However, in the results of Guyer and Voorhees, the stress driven instabilities can be suppressed only for films under tensile strain ($\epsilon^* < 0$), while for compressive layers this stabilization by high V is not possible and then systems are always unstable. This is different from our results where films of both $\epsilon^* > 0$ and $\epsilon^* < 0$ can be stabilized for symmetric or asymmetric cases, as shown in Figs. 3 and 4.

Compared to single-component film, one of the additional and crucial factors for alloy film stability is η , reflecting the compositional stress caused by different atomic sizes of alloy components. From the model of Guyer and Voorhees^{8,9,10,11} it is found that the compositional stress can stabilize the film modulations. However, recent study of Spencer *et al.*^{12,13,14} shows that when one considers single atomic mobility, the coupling of solute strain (η) and film-substrate misfit strain ϵ always enhances the instability and makes the alloy film more unstable than the single-component film, and only for the case of unequal surface mobilities can the solute strain lead to a decrease of the film instability with a possibility of stabilizing the system through deposition. Here we have used one effective surface mobility to describe the dynamics of the alloy film, but have more complicated and different results for the role of solute stress (or η). To obtain the effect of η more clearly, without the interplay of composition dependence of elastic constants, we consider the case of $E_1^* = \mu_1^* = 0$, corresponding to Figs. 3 (a), (c) and 4 (a). These three diagrams show that the joint morphological and compositional instabilities can be suppressed by large deposition rate, as discussed above, resulting in less unstable film compared with single-component system where the Asaro-Tiller-Grinfeld morphological instability (as described in Eq. (43)) always occurs for any deposition rate. In this sense our result is in agreement with that of Guyer and Voorhees. However, in the presence of solute stress the diagrams in Figs. 3 and 4 exhibit the smaller stable regions for larger η^* , corresponding to the destabilizing effect of large compositional strain, which is opposite to the effect found by Guyer and Voorhees but similar to that of Spencer *et al.*. A new feature of our results is in the stability diagrams for $T > T_c^{\text{eff}}$, *i.e.* Figs. 3 (a) and 4 (a), where the system is always stable for

small misfits $|\epsilon^*| < \epsilon_0^*$ when $\eta^* < \eta_c^*$, with η_c^* defined in Eq. (47) and ϵ_0^* dependent on the value of η^* . Thus, only when the compositional stress exceeds a critical value, *i.e.* $\eta^* > \eta_c^*$, can the instability of the film be significantly enhanced. This is different from all the previous results, and can be explained by Eq. (47) in the limit of zero misfit, which shows analytically that a film is stable against any disturbance when $\eta^* < \eta_c^*$. This feature does not exist for $T < T_c^{\text{eff}}$, which can also be expected from the stability condition (48) for $\epsilon^* = 0$.

VI. KINETIC CRITICAL THICKNESS

According to the stability calculations shown above, in general the morphological and compositional modes are coupled, that is, instability in one also implies instability in the other, and then the joint stability or instability is determined by diagrams illustrated in Figs. 3 and 4. However, in some experiments, although the chosen material parameters and experimental conditions correspond to the unstable region of our theoretical diagram, the film profiles are in fact observed to be stable. This may be due to the kinetic stabilization effect of growing film, as proposed by Spencer *et al.*^{15,16} When the real part of perturbation growth rate σ is positive, the instability develops and grows with time. However, at early time of growth the surface perturbations have not enough time to develop and become observable compared to constant deposition of materials flux. Only after a sufficient time, that is, when the film is thick enough, can the perturbations develop substantially and be apparent relative to the planar basic state of the film. Then the perturbation growth rate (σ) can exceed the relative growth rate of the film basic state (v/\bar{h}). Thus, this competition between deposition and perturbation growth results in a kinetic critical thickness h_c , with the nondimensional form given by

$$h_c^* = V/\sigma \quad (52)$$

in linear analysis,^{12,15,16} where σ is usually approximated by the maximum perturbation growth rate σ_{max} with respect to different growing mode k . Below this critical thickness h_c , the instability of the growing film is effectively suppressed by deposition flux and may not be seen experimentally, while above h_c the surface undulations are seen. This phenomenon for the onset of stress driven instability at certain film thickness has been observed by experiments, for both the systems of SiGe^{26,28} and InGaAs.^{35,36,37}

From the mechanism of kinetic stabilization described above, one can expect that kinetic critical thickness h_c^* will increase with deposition rate, which is verified by our calculations of h_c^* versus V shown in Fig. 5 for growth temperature $T > T_c^{\text{eff}}$. For both the SiGe-type and InGaAs-type parameters, the log-log plots in Figs. 5 (a) and (b) show that when the rescaled deposition rate V is not large (corresponding to most experimental cases), generally the relationship between h_c^* and V is not linear, and the nature of the rise of h_c^* with V for compressive and tensile misfits is different for the case of composition dependent elastic moduli. At sufficiently high deposition rate, the curves of h_c^* for opposite signs of misfit ϵ^* and for different composition dependent forms of elastic moduli converge, and its variation with respect to deposition rate is linear, which can be seen on scale of V larger than that of Fig. 5 but is not shown here. These properties imply that the maximum of perturbation growth rate σ depends on small deposition rate V as well as on the values of E_1^* and μ_1^* , but is independent of them when V is large enough.

From the plots in Fig. 5 we can also obtain the results of stability asymmetry with respect to the sign of misfit, except for large enough deposition rate V which results in the presence of symmetry of h_c in ϵ . For SiGe-type system with composition dependent elastic moduli, Fig. 5 (a) shows that kinetic critical thickness for compressive films ($\epsilon^* > 0$) is smaller than that of tensile films ($\epsilon^* < 0$) when V is not large enough, corresponding to the phenomenon that the growing films under tension are effectively more stable, as observed in SiGe experiments.²³ The asymmetric property for InGaAs-type system is more complicated, that is, it depends on the deposition rate for $T > T_c^{\text{eff}}$, as shown in Fig. 5 (b). For intermediate values of V , the compressive films have larger h_c^* compared to the films under tension, making compressive films more stable. For small V , h_c^* of compressive films is smaller, leading to less effective stability which is similar to SiGe-type films. Note that the asymmetric property obtained here for InGaAs is different from the result of higher η^* values shown in the stability diagram of Fig. 4 (b), which in fact represents the asymmetry of absolute stability, but not that of effectively kinetic stabilization discussed here.

This deposition dependent behavior of asymmetry for InGaAs films can qualitatively explain the contradiction in recent experimental observations. In the experiment of Okada *et al.*,³¹ compressively strained layers are found to be more stable than tensile layers, whereas the observation of Guyer *et al.*³⁴ yields opposite result. According to our calculations here, this inconsistency is attributed to different deposition rate used in these experiments: The growth conducted by Guyer *et al.* has much lower deposition rate and then corresponds to the asymmetry similar to SiGe films but opposite to that of Okada *et al.*. The direct measurement of critical thickness for the onset of instability has been carried out by Gendry *et al.*³⁵ for different signs of misfit and different deposition rate. Since our calculations mainly focus on 50-50 mixture, different from the alloy concentrations used in Ref. 35, here we only compare the theoretical and experimental results qualitatively. As observed during MBE growth of Gendry *et al.*, for the undoped

layers with As-stabilized surface showing strong (2×4) reconstruction, the critical thickness in compression is found to be less than that in tension when deposition rate is small, while for high deposition rate, larger h_c in compression is obtained. This is consistent with our findings in Fig. 5 (b) for the case of composition dependent elastic moduli.

The scaling behavior for critical thickness h_c with respect to misfit ϵ has also attracted attention in recent work. Since the system becomes more unstable with the increase of misfit strain, h_c is expected to decrease with larger ϵ . For single-component, lattice mismatched films, where the effect of solute stress is absent, the kinetic critical thickness is found to follow the ϵ^{-8} power law.^{15,16} Our calculations also lead to ϵ^{-8} power law as follows: From Eq. (52), $h_c^* = V/\sigma_{\max}$; from Eq. (43), one can show that the maximum growth rate occurs at $k_{\max} = 3\epsilon^{*2}/4\gamma^*$ which leads to $h_c^* = (256\gamma^{*3}V)/(27\epsilon^{*8})$. The observed behavior for multi-component system like SiGe is different. The experiment carried out by Perović *et al.*²⁶ finds that kinetic critical thickness h_c for coherent SiGe/Si(100) varies with misfit as ϵ^{-4} , while recent observation of Tromp *et al.*²⁸ found a much slower dependence ϵ^{-1} . Our results for the dependence of rescaled critical thickness h_c^* on ϵ^* are shown in Fig. 6, and indicate that generally the scaling of h_c^* versus ϵ^* is not a power law. For the SiGe-type system, as illustrated in Fig. 6 (a), the curve (dotted) for the case of composition independent elastic moduli ($E_1^* = \mu_1^* = 0$) presents a behavior close to $1/\epsilon^{*8}$ for large misfit ϵ^* , but has slower decreasing form for small ϵ^* . When we consider the composition dependence of elastic constants ($E_1^* \neq 0$ and $\mu_1^* \neq 0$), the decrease of h_c^* with ϵ^* is slightly faster than ϵ^{*-8} for the compressive layers ($\epsilon^* > 0$), but much slower for the tensile films. In Fig. 6 (b), corresponding to the InGaAs-type case, h_c^* scales similar to ϵ^{*-8} only for small misfit ϵ^* , but decreases much slower at larger values of misfit, in particular for films grown under tension if $E_1^* \neq 0$ and $\mu_1^* \neq 0$.

The asymmetry of effective stability (*i.e.* thickness h_c) with respect to the sign of misfit can also be seen in Fig. 6 for the case of composition dependent elastic moduli. For the SiGe-type system (Fig. 6 (a)) h_c^* for tensile films is always larger than that of compressive films, that is, tensile layers are effectively more stable, as found earlier. However, the InGaAs-type system yields more complicated scaling behavior. For large misfit ϵ^* , Fig. 6 (b) exhibits that films under tension have higher h_c^* , and then can be observed as more stable, similar to the result of Fig. 6 (a). This is in accord with the result of h_c^* versus V shown in Fig. 5 (b), since here the rescaled deposition rate V is chosen as 10^{-3} , corresponding to the small V region of Fig. 5 (b) where one has large $|\epsilon^*| = 0.8$ and SiGe-like behavior of asymmetry. For intermediate values of $|\epsilon^*|$, asymmetry opposite to SiGe-type system is obtained, that is, the h_c^* curve for compressive layers lies above that for tensile layers, resulting in more stable compressive films. When $|\epsilon^*|$ gets smaller (not shown here), the difference of h_c^* values between $\epsilon^* > 0$ and $\epsilon^* < 0$ becomes negligible, and then we have the symmetry of stability for films under compression and under tension even when elastic constants depend on composition field. Therefore, combining Figs. 5 (b) and 6 (b), we conclude that the asymmetry of effective stabilization for InGaAs-type films is dependent on both the deposition rate and the magnitude of misfit strain.

VII. CONCLUSIONS

In this paper, we have determined the stability properties for growth of dislocation-free and coherent, strained alloy films by developing a continuum dynamical model and performing a linear stability analysis. In our model there are two important and new features, the coupling between top surface of the film and the bulk underneath, and the composition dependence of elastic moduli (E and μ), which result in new stability results. Both the thermodynamics and elastic effects are considered. Besides the phase separation mechanism at low temperature and the role of surface energy that favours the planar surface, we also include the effects of elasticity which can arise due to (i) the mismatch of lattice constant between a growing film and the substrate, resulting in nonzero misfit strain ϵ ; (ii) the dependence of lattice constant on composition, leading to nonzero solute strain represented by a coefficient η ; and (iii) the dependence of elastic moduli on composition, as given in Eq. (8). Moreover, the deposition rate can play an important role for the growing films. The main results, due to the interplay of these factors, that we obtain can be summarized as follows.

For single-component epitaxial growth, when one studies the stability of the free surface of a growing film, the morphological corrugation may lead to the formation of coherent islands. This occurs on account of the misfit strain caused by lattice mismatch. In contrast, for multi-component growth like MBE, the time evolution of the morphological profile is coupled to the dynamics of composition. Physically the coupling occurs since smaller (larger) atoms of the film prefer to incorporate in regions of compressive (tensile) stress. This leads smaller atoms to preferentially diffuse to troughs (peaks) and larger atoms to segregate to peaks (troughs), for a film under compression (tension). As a result of the coupling, there is a joint modulation of the surface morphological profile and the alloy composition, as well as a common perturbation growth rate σ (see Eqs. (38), (39), and (40)). Thus a planar surface can be stabilized only if alloy decomposition is suppressed and vice versa. Some experiments (SiGe²⁹ and InGaAs^{31,32,33}) have verified such a simultaneous development of morphological and compositional modulations.

For *bulk* strained alloys, the compositional profile is homogeneous above the bulk coherent spinodal temperature T_c^{eff} , and the decomposition can occur only below T_c^{eff} . However, for multi-component epitaxial *films*, alloy decomposition

occurs both theoretically and experimentally even for temperature T higher than T_c^{eff} . This is due to two major effects. First, due to the coupling between morphological and compositional profiles, the phase separation can be driven by the difference in strain energy densities along the surface caused by the morphological undulation. Even in the absence of η , that is, when the atomic size difference is negligible, the composition dependence of the film elastic constants can be the cause of coupling between morphology h and composition ϕ , as shown in Eqs. (44) and (45) for special case of $\epsilon^* \neq 0$ but $\eta^* = 0$. The second effect is related to solute stress (or η) itself. As depicted in Eqs. (46) and (47) for $\epsilon^* = 0$ and $\eta^* \neq 0$, when the morphological and compositional degrees of freedom are decoupled and we have stable surface morphology, alloy decomposition can also occur for $T > T_c^{\text{eff}}$ if η^* is large enough. This means that when the solute stress is too strong, corresponding to very large difference in the atomic sizes of alloy components, the small and large species prefer to segregate with respect to very small background disturbances of surface profile.

This compositional instability, as well as the morphological modulation, can be completely suppressed by high deposition rate, both for T above and below coherent spinodal T_c^{eff} , as seen in the stability diagrams of Figs. 3 and 4 as well as from the analytic results derived for special cases in Sec. V A. Generally, increasing the magnitude of misfit ϵ increases the instability, and larger solute strain (η^*) also enhances the instability for most of the cases. Furthermore, the nonphysical short wavelength instability is absent in our work, due to the consideration of gradient free energy.

Including the coupling between film surface and underlying bulk has resulted in some interesting results. One of the new features is on the role of η . Our analysis naturally brings a critical value η_c^* for the stability at temperature $T > T_c^{\text{eff}}$. For $|\eta^*|$ below η_c^* , the system is always stable within a range of misfit ϵ^* , regardless of any deposition rate V . Only for $|\eta^*| > \eta_c^*$ can the increase of η^* significantly enhance the instability; this is shown in Eq. (47) and Fig. 2 for $\epsilon^* = 0$, as well as in Figs. 3 and 4 for nonzero ϵ^* . When the surface-bulk coupling is neglected, the stability results do not have any critical η^* . Our results for the scaling behavior of kinetic critical thickness h_c (the growing film is effectively stabilized by deposition up to thickness h_c) are also different from earlier work. In general, the dependence of nondimensional critical thickness h_c^* on rescaled deposition rate V is not linear for intermediate and small V (corresponding to most experimental cases), and its dependence on rescaled misfit ϵ^* is not necessarily a power law, as shown in Figs. 5 and 6 respectively, even for $E_1^* = \mu_1^* = 0$.

The asymmetry of stability with respect to the sign of misfit ϵ^* is found in the systems with composition dependent film elastic moduli, while for the composition independent case ($E_1^* = \mu_1^* = 0$), it is absent. Figures 3 and 4 show the diagrams for absolute stability. For SiGe-type system, the films grown under tension ($\epsilon^* < 0$) are expected to be more stable than those under compression ($\epsilon^* > 0$), while the form of asymmetry is opposite for InGaAs-type films. For the effective stabilization, as measured by critical thickness h_c , the asymmetry can also be found unless the deposition rate is too large. According to our calculations, a tensile film, with SiGe-type parameters, will be observed as stable up to a thickness larger than that for a compressive film, as shown in Figs. 5 (a) and 6 (a). However, for InGaAs-type system the asymmetry depends on both the deposition rate and the magnitude of misfit. As found in Fig. 5 (b), the system will have asymmetry similar to SiGe-type at small V , but for intermediate values of V reverse asymmetry is obtained, and then the compressive films are effectively more stable. This can explain the observations of recent experiments on InGaAs epitaxial films.^{31,34,35} When the deposition rate is fixed, the forms of asymmetry is opposite for large and intermediate magnitude of misfit ϵ^* , but at small misfit the symmetry with respect to the sign of ϵ^* is obtained (see Fig. 6 (b)).

As discussed above and shown in Figs. 2–6, the stability properties and asymmetry depend on the chosen material system and the experimental conditions (such as deposition rate v and growth temperature T). E.g., if we desire a system with very strong modulations, stability diagrams (Figs. 3 and 4) and the variation of kinetic critical thickness (Figs. 5 and 6) show that the instability requires large misfit ϵ , large solute coefficient η , small deposition rate v , and large enough film thickness. Also note that the stability results presented here are with respect to dimensionless parameters V , ϵ^* , η^* , and γ^* , which are all temperature dependent according to Eqs. (36), (33), and (34), via the coefficients r and Γ_ϕ . The explicit temperature dependence of $\Gamma_\phi = \Gamma_h/\delta$ is given after Eq. (2). Thus, even when we already choose the growing system with fixed material parameters, the stability behavior will vary with growth temperature, through the variation of the dimensionless parameters.

All of the above results show that the problem of multi-component epitaxial growth, which is essentially a problem of nonequilibrium, is rich in interesting physics. It involves competition between thermodynamics and deposition, and coupling between morphology and composition. More interesting and richer results can be obtained if one further studies the detailed patterns and structures of the growing film, beyond the early evolution regime considered in this paper.

Acknowledgments

This work was supported by the NSERC of Canada.

APPENDIX A: GENERAL RESULTS FOR MECHANICAL EQUILIBRIUM EQUATION

As discussed in Sec. III, the mechanical equilibrium equation for the film is considered to zeroth order of elastic constants, and then it is linear with the expansion form:

$$(1 - 2\nu_0^f)(\partial_z^2 - q^2) \begin{bmatrix} \hat{u}_x^f \\ \hat{u}_y^f \\ \hat{u}_z^f \end{bmatrix} + \begin{bmatrix} iq_x \\ iq_y \\ \partial_z \end{bmatrix} \left[iq_x \hat{u}_x^f + iq_y \hat{u}_y^f + \partial_z \hat{u}_z^f - 2(1 + \nu_0^f)\eta\hat{\phi} \right] = 0. \quad (\text{A1})$$

The corresponding general solution is

$$\begin{aligned} \hat{u}_i^f = & \begin{bmatrix} \alpha_x \\ \alpha_y \\ \alpha_z \end{bmatrix} \cosh(qz) + \begin{bmatrix} \beta_x \\ \beta_y \\ \beta_z \end{bmatrix} \sinh(qz) \\ & - \begin{bmatrix} Ciq_x/q \\ Ciq_y/q \\ D \end{bmatrix} z \sinh(qz) - \begin{bmatrix} Diq_x/q \\ Diq_y/q \\ C \end{bmatrix} z \cosh(qz) + \left(\frac{1 + \nu_0^f}{1 - \nu_0^f} \right) \eta \begin{bmatrix} iq_x \hat{W} \\ iq_y \hat{W} \\ \partial_z \hat{W} \end{bmatrix}, \end{aligned} \quad (\text{A2})$$

with \hat{W} defined by Eq. (24) of Sec. III and

$$\begin{aligned} C &= \frac{1}{3 - 4\nu_0^f} (iq_x \alpha_x + iq_y \alpha_y + q\beta_z), \\ D &= \frac{1}{3 - 4\nu_0^f} (iq_x \beta_x + iq_y \beta_y + q\alpha_z). \end{aligned} \quad (\text{A3})$$

The equation for the substrate displacement is similar to Eq. (A1) but with $\hat{\phi}$ equal to zero. Considering the boundary condition (19) for the decay of strains far from the interface, we have the solution form

$$\hat{u}_i^s = \begin{bmatrix} u_x^0 \\ u_y^0 \\ u_z^0 \end{bmatrix} e^{qz} - \begin{bmatrix} iq_x/q \\ iq_y/q \\ 1 \end{bmatrix} B z e^{qz}, \quad (\text{A4})$$

where

$$B = \frac{1}{3 - 4\nu^s} (iq_x u_x^0 + iq_y u_y^0 + q u_z^0). \quad (\text{A5})$$

The expression of stresses and strains can then be obtained through the above solutions, e.g.,

$$\begin{aligned} \hat{u}_{ll}^f &= 2(1 - 2\nu_0^f) [C \cosh(qz) + D \sinh(qz)] + \left(\frac{1 + \nu_0^f}{1 - \nu_0^f} \right) \eta \hat{\phi}, \\ \hat{u}_{zz}^f &= q [\alpha_z \sinh(qz) + \beta_z \cosh(qz)] - (D + Cqz) \sinh(qz) \\ &\quad - (C + Dqz) \cosh(qz) + \left(\frac{1 + \nu_0^f}{1 - \nu_0^f} \right) \eta \partial_z^2 \hat{W}, \end{aligned} \quad (\text{A6})$$

which are used in the elastic free energy calculation of Sec. IV.

From linearized boundary conditions (16)–(18) at film surface and film-substrate interface, as well as the consideration that both $\hat{\phi}$ and \hat{W} are zero at $z = \bar{\zeta} = 0$, we can determine the parameters α_i , β_i , u_i^0 , and then C , D , and B in term of \hat{h} , $\hat{\zeta}$ and values $\hat{\phi}$ or \hat{W} evaluated at $z = \bar{h}$. Here we omit the tedious deduction process and only present the results, which are:

$$\begin{aligned} iq_x \alpha_x + iq_y \alpha_y = & A^{-1} \rho e^f \left\{ q \bar{u} \hat{\zeta} [-e^s e^f - (b^s - \rho c^s)(q\bar{h} - \sinh(q\bar{h}) \cosh(q\bar{h})) - e^s \sinh^2(q\bar{h})] \right. \\ & + \left[q \bar{u} \hat{h} + \left(\frac{1 + \nu_0^f}{1 - \nu_0^f} \right) \eta q (\partial_z \hat{W})_{z=\bar{h}} \right] [e^s e^f \cosh(q\bar{h}) \\ & + (b^s b^f + \rho c^s) \sinh(q\bar{h}) + (b^s - \rho c^s) q \bar{h} \cosh(q\bar{h}) - e^s q \bar{h} \sinh(q\bar{h})] \\ & + \left(\frac{1 + \nu_0^f}{1 - \nu_0^f} \right) \eta (\partial_z^2 \hat{W} - \hat{\phi})_{z=\bar{h}} [-b^s e^f \cosh(q\bar{h}) \\ & \left. - e^s b^f \sinh(q\bar{h}) + e^s q \bar{h} \cosh(q\bar{h}) + (-b^s + \rho c^s) q \bar{h} \sinh(q\bar{h})] \right\}, \end{aligned} \quad (\text{A7})$$

$$\begin{aligned}
iq_x\beta_x + iq_y\beta_y = & A^{-1} \left\{ q\bar{u}\hat{\zeta} \left[-(1 + \rho b^s)e^f b^f + (1 + 2\rho b^s - \rho^2 c^s)q^2 \bar{h}^2 \right. \right. \\
& + \rho e^s e^f (q\bar{h} + \sinh(q\bar{h}) \cosh(q\bar{h})) + (-\rho b^s e^f + \rho^2 c^s e^f) \sinh^2(q\bar{h}) \\
& + \left[q\bar{u}\hat{h} + \left(\frac{1 + \nu_0^f}{1 - \nu_0^f} \right) \eta q \left(\partial_z \hat{W} \right)_{z=\bar{h}} \right] [e^f (c^f + \rho b^s b^f) \cosh(q\bar{h}) \\
& + \rho e^s e^{f^2} \sinh(q\bar{h}) - \rho e^s e^f q\bar{h} \cosh(q\bar{h}) - (c^f + 2\rho b^s p^f - \rho^2 c^s b^f) q\bar{h} \sinh(q\bar{h})] \\
& + \left(\frac{1 + \nu_0^f}{1 - \nu_0^f} \right) \eta \left(\partial_z^2 \hat{W} - \hat{\phi} \right)_{z=\bar{h}} [-\rho e^s e^f b^f \cosh(q\bar{h}) \\
& + (-c^f b^f + \rho b^s (2 - 4\nu_0^{f^2}) - \rho^2 c^s b^f) \sinh(q\bar{h}) \\
& + (c^f + 2\rho b^s p^f - \rho^2 c^s b^f) q\bar{h} \cosh(q\bar{h}) + \rho e^s e^f q\bar{h} \sinh(q\bar{h})] \left. \right\}, \tag{A8}
\end{aligned}$$

$$\begin{aligned}
q_y \alpha_x &= q_x \alpha_y, \\
q_y \beta_x &= q_x \beta_y, \tag{A9}
\end{aligned}$$

$$\begin{aligned}
q\alpha_z = & A^{-1} \left\{ q\bar{u}\hat{\zeta} \left[-(1 + \rho b^s)e^{f^2} - (1 + 2\rho b^s - \rho^2 c^s)q^2 \bar{h}^2 \right. \right. \\
& - \rho e^s e^f (q\bar{h} + \sinh(q\bar{h}) \cosh(q\bar{h})) - (c^f + 2\rho b^s p^f - \rho^2 c^s b^f) \sinh^2(q\bar{h}) \\
& + \left[q\bar{u}\hat{h} + \left(\frac{1 + \nu_0^f}{1 - \nu_0^f} \right) \eta q \left(\partial_z \hat{W} \right)_{z=\bar{h}} \right] \rho e^f [b^s e^f \cosh(q\bar{h}) \\
& + e^s b^f \sinh(q\bar{h}) + e^s q\bar{h} \cosh(q\bar{h}) + (-b^s + \rho c^s) q\bar{h} \sinh(q\bar{h})] \\
& + \left(\frac{1 + \nu_0^f}{1 - \nu_0^f} \right) \eta \left(\partial_z^2 \hat{W} - \hat{\phi} \right)_{z=\bar{h}} \rho e^f [-e^s e^f \cosh(q\bar{h}) \\
& - (b^s b^f + c^s \rho) \sinh(q\bar{h}) + (b^s - c^s \rho) q\bar{h} \cosh(q\bar{h}) - e^s q\bar{h} \sinh(q\bar{h})] \left. \right\}, \tag{A10}
\end{aligned}$$

$$\begin{aligned}
q\beta_z = & A^{-1} \left\{ q\bar{u}\hat{\zeta} [-\rho e^s e^f b^f - (c^f + 2\rho b^s p^f - \rho^2 c^s b^f)(q\bar{h} - \sinh(q\bar{h}) \cosh(q\bar{h})) \right. \\
& + \rho e^s e^f \sinh^2(q\bar{h})] + \left[q\bar{u}\hat{h} + \left(\frac{1 + \nu_0^f}{1 - \nu_0^f} \right) \eta q \left(\partial_z \hat{W} \right)_{z=\bar{h}} \right] \\
& \times [\rho e^s e^f b^f \cosh(q\bar{h}) + (c^f b^f - \rho b^s (2 - 4\nu_0^{f^2}) + \rho^2 c^s b^f) \sinh(q\bar{h}) \\
& + (c^f + 2\rho b^s p^f - \rho^2 c^s b^f) q\bar{h} \cosh(q\bar{h}) + \rho e^s e^f q\bar{h} \sinh(q\bar{h})] \\
& + \left(\frac{1 + \nu_0^f}{1 - \nu_0^f} \right) \eta \left(\partial_z^2 \hat{W} - \hat{\phi} \right)_{z=\bar{h}} [-e^f (c^f + \rho b^s b^f) \cosh(q\bar{h}) - \rho e^s e^{f^2} \sinh(q\bar{h}) \\
& - \rho e^s e^f q\bar{h} \cosh(q\bar{h}) - (c^f + 2\rho b^s p^f - \rho^2 c^s b^f) q\bar{h} \sinh(q\bar{h})] \left. \right\}, \tag{A11}
\end{aligned}$$

and

$$\begin{aligned}
C = & A^{-1} \left\{ q\bar{u}\hat{\zeta} [-\rho e^s e^f - (1 + 2\rho b^s - \rho^2 c^s)(q\bar{h} - \sinh(q\bar{h}) \cosh(q\bar{h})) \right. \\
& + \left[q\bar{u}\hat{h} + \left(\frac{1 + \nu_0^f}{1 - \nu_0^f} \right) \eta q \left(\partial_z \hat{W} \right)_{z=\bar{h}} \right] [\rho e^s e^f \cosh(q\bar{h}) \\
& + (b^f - 2\rho b^s \nu_0^f + \rho^2 c^s) \sinh(q\bar{h}) + (1 + 2\rho b^s - \rho^2 c^s) q\bar{h} \cosh(q\bar{h})] \\
& + \left(\frac{1 + \nu_0^f}{1 - \nu_0^f} \right) \eta \left(\partial_z^2 \hat{W} - \hat{\phi} \right)_{z=\bar{h}} [-e^f (1 + \rho b^s) \cosh(q\bar{h}) \\
& - \rho e^s e^f \sinh(q\bar{h}) - (1 + 2\rho b^s - \rho^2 c^s) q\bar{h} \sinh(q\bar{h})] \left. \right\}, \tag{A12}
\end{aligned}$$

$$\begin{aligned}
D = & A^{-1} \left\{ q\bar{u}\hat{\zeta} \left[-e^f(1 + \rho b^s) - (1 + 2\rho b^s - \rho^2 c^s) \sinh^2(q\bar{h}) \right] \right. \\
& + \left[q\bar{u}\hat{h} + \left(\frac{1 + \nu_0^f}{1 - \nu_0^f} \right) \eta q \left(\partial_z \hat{W} \right)_{z=\bar{h}} \right] \left[e^f(1 + \rho b^s) \cosh(q\bar{h}) \right. \\
& + \rho e^s e^f \sinh(q\bar{h}) - (1 + 2\rho b^s - \rho^2 c^s) q\bar{h} \sinh(q\bar{h})] \\
& + \left(\frac{1 + \nu_0^f}{1 - \nu_0^f} \right) \eta \left(\partial_z^2 \hat{W} - \hat{\phi} \right)_{z=\bar{h}} \left[-\rho e^s e^f \cosh(q\bar{h}) \right. \\
& \left. \left. - (b^f - 2\rho b^s \nu_0^f + \rho^2 c^s) \sinh(q\bar{h}) + (1 + 2\rho b^s - \rho^2 c^s) q\bar{h} \cosh(q\bar{h}) \right] \right\}, \tag{A13}
\end{aligned}$$

for the film solution, as well as

$$\begin{aligned}
u_x^0 &= \alpha_x, \\
u_y^0 &= \alpha_y, \\
u_z^0 &= \bar{u}\hat{\zeta} + \alpha_z,
\end{aligned} \tag{A14}$$

and

$$B = \left(q\bar{u}\hat{\zeta} + iq_x\alpha_x + iq_y\alpha_y + q\alpha_z \right) / c^s, \tag{A15}$$

for the substrate solution. In equations (A7)–(A13),

$$\begin{aligned}
A = & e^{f^2} + (1 + 2\rho b^s - \rho^2 c^s) q^2 \bar{h}^2 \\
& + 2\rho e^s e^f \sinh(q\bar{h}) \cosh(q\bar{h}) + (c^f + 2\rho b^s b^f + \rho^2 c^s) \sinh^2(q\bar{h}),
\end{aligned} \tag{A16}$$

where ρ is the relative film-substrate stiffness:

$$\rho = \mu_0^f / \mu^s, \tag{A17}$$

and the elastic parameters $e^{f(s)}$, $b^{f(s)}$, $c^{f(s)}$, and $p^{f(s)}$ are expressed by

$$\begin{aligned}
e^f &= 2(1 - \nu_0^f) & \text{and} & & e^s &= 2(1 - \nu^s), \\
b^f &= 1 - 2\nu_0^f & \text{and} & & b^s &= 1 - 2\nu^s, \\
c^f &= 3 - 4\nu_0^f & \text{and} & & c^s &= 3 - 4\nu^s, \\
p^f &= 2 - 3\nu_0^f & \text{and} & & p^s &= 2 - 3\nu^s.
\end{aligned} \tag{A18}$$

To check whether these results are correct, we compare them with the known solutions by taking appropriate limits. For the single-component system with planar film-substrate interface and different elastic constants between film and substrate, Spencer et al.¹⁵ have given the corresponding solution, which can be recovered by setting $\hat{\zeta} = 0$ as well as all the terms related to $\hat{\phi}$ and \hat{W} to be zero in the above formulae (A7)–(A16). While for binary alloy system ($\hat{\phi} \neq 0$) but with identical elastic constants for film and substrate as well as flat interface, the solution can be obtained by setting $\rho = 1$, $\nu_0^f = \nu^s = \nu_0$, $e^f = e^s$, $b^f = b^s$, $c^f = c^s$, $p^f = p^s$, and $\hat{\zeta} = 0$ in the above equations. The corresponding results are presented in Eqs. (20)–(23) of Sec. III, and consistent with that of previous work.²⁰

APPENDIX B: ELASTIC FREE ENERGY IN FOURIER EXPANSION

Using the Fourier expansion form (15), the elastic free energy functional (26) can be expanded as

$$\mathcal{F}_{\text{el}}^f = \int_0^h d^3r \left[\bar{\mathcal{E}}^f + \sum_{\mathbf{q}} e^{i(q_x x + q_y y)} \hat{\mathcal{E}}^f(\mathbf{q}, z, t) \right] + \tilde{\mathcal{F}}_{\text{el}}^f, \tag{B1}$$

with the zeroth order quantity

$$\bar{\mathcal{E}}^f = \frac{E_0}{1 - \nu_0} \epsilon^2, \tag{B2}$$

which has no contribution to dynamic equations (2) and (3), and the first order term

$$\hat{\mathcal{E}}^f = \frac{E_0}{1-\nu_0} \epsilon \left[-\hat{u}_{ll}^f + \hat{u}_{zz}^f + \left(2\eta + \frac{2E_1^* - (1+\nu_0)\mu_1^*}{1-\nu_0} \epsilon \right) \hat{\phi} \right], \quad (\text{B3})$$

which is used in evaluating the linear form of Eq. (2) for the surface height evolution. For the purpose of performing the linear analysis on Eq. (3) for the evolution of ϕ , we should use the second order elastic free energy $\tilde{\mathcal{F}}_{\text{el}}^f$:

$$\begin{aligned} \tilde{\mathcal{F}}_{\text{el}}^f = & \sum_{\mathbf{q}} \int_0^{\bar{h}} dz \left\{ \frac{E_0}{1-2\nu_0} \left[\left(\frac{3}{2}\eta^2 + \frac{2(3E_1^* - 2(1+\nu_0)\mu_1^*)}{1-\nu_0} \epsilon \eta \right) \hat{\phi}(\mathbf{q})\hat{\phi}(-\mathbf{q}) \right. \right. \\ & - \left(\eta + \frac{2E_1^* - (1+2\nu_0)\mu_1^*}{1-\nu_0} \epsilon \right) \hat{\phi}(\mathbf{q})\hat{u}_{ll}^f(-\mathbf{q}) + \frac{\nu_0}{2(1+\nu_0)} \hat{u}_{ll}^f(\mathbf{q})\hat{u}_{ll}^f(-\mathbf{q}) \\ & \left. \left. + \frac{E_0}{1-\nu_0} \mu_1^* \epsilon \hat{\phi}(\mathbf{q})\hat{u}_{zz}^f(-\mathbf{q}) + \frac{E_0}{2(1+\nu_0)} \hat{u}_{ij}^f(\mathbf{q})\hat{u}_{ij}^f(-\mathbf{q}) \right\}, \end{aligned} \quad (\text{B4})$$

which is different from the result in Ref. 20 where surface-bulk coupling of the film is neglected and the second order elastic energy is evaluated at top surface $z = \bar{h}$. If we calculate the functional differentiation $\delta\mathcal{F}_{\text{el}}^f/\delta\phi$ in Fourier space (that is, $\delta\mathcal{F}_{\text{el}}^f/\delta\hat{\phi}(-\mathbf{q}, z, t)$) using Eq. (B4), we can also obtain the formula (30) of Sec. IV derived through real space procedure.

The expressions for first order elastic energy density (B3) evaluated at the surface and the functional differentiation Eq. (30) in terms of \hat{h} and $\hat{\phi}_s$ can be obtained by using the strain tensor formula (A6) of Appendix A and substituting the form of \hat{W} derived in Sec. IV, *i.e.* $\hat{W} = v^2\hat{\phi}/(\Omega^2 - q^2v^2)$, into the solution of mechanical equilibrium equation (20)–(23) (with the approximation $\hat{\phi}|_{z=\bar{h}} = \hat{\phi}_s$ to first order). They are given by

$$\hat{\mathcal{E}}^f|_s = \frac{E_0}{1-\nu_0} \epsilon \left[-2(1+\nu_0)\epsilon q\hat{h} + \left(2\eta \frac{\Omega - \nu_0 qv}{\Omega + qv} + \frac{2E_1^* - (1+\nu_0)\mu_1^*}{1-\nu_0} \epsilon \right) \hat{\phi}_s \right], \quad (\text{B5})$$

and

$$\begin{aligned} \left(\nabla^2 \frac{\delta\mathcal{F}_{\text{el}}^f}{\delta\phi} \right) \bigg|_{\mathbf{q}|_s} = & q^2 \frac{2E_0}{1-\nu_0} \left\{ \left(\frac{1+\nu_0}{1-\nu_0} \right) q \left[(1-2\nu_0)\epsilon\eta + (2E_1^* - (1+\nu_0)\mu_1^*)\epsilon^2 \right] \hat{h} \right. \\ & - \left[\eta^2 + \frac{8E_1^* - 5(1+\nu_0)\mu_1^*}{2(1-\nu_0)} \epsilon\eta \right. \\ & \left. \left. - \left(\frac{1+\nu_0}{1-\nu_0} \right) \left[(1-2\nu_0)\eta^2 + (2E_1^* - (1+\nu_0)\mu_1^*)\epsilon\eta \right] \frac{qv}{\Omega + qv} \right] \hat{\phi}_s \right\}, \end{aligned} \quad (\text{B6})$$

respectively. Note that for the case of composition independent elastic moduli ($E_1^* = \mu_1^* = 0$), Eq. (B5) yields a result for first order elastic energy density which is the same as that in Ref. 20. The differences occur in Eq. (B6) due to differences in $\tilde{\mathcal{F}}_{\text{el}}^f$ as well as different model and derivation procedure: In the previous work of Ref. 20, the second order elastic energy (B4) is evaluated at surface $z = \bar{h}$ first and expressed in terms of \hat{h} and $\hat{\phi}|_{z=\bar{h}}$, and then the functional differentiation is carried out directly on surface ϕ with an approximation that $\delta\tilde{\mathcal{F}}_{\text{el}}^f/\delta\hat{\phi}_s \sim \delta\tilde{\mathcal{F}}_{\text{el}}^f/\delta\hat{\phi}|_{z=\bar{h}}$.

* Electronic address: zfh@physics.utoronto.ca

† Electronic address: desai@physics.utoronto.ca; URL: <http://www.physics.utoronto.ca/people/faculty/desai.html>

¹ R. J. Asaro and W. A. Tiller, Metall. Trans. **3**, 1789 (1972).

² M. A. Grinfeld, Sov. Phys. Dokl. **31**, 831 (1987).

³ D. J. Srolovitz, Acta Metall. **37**, 621 (1989).

⁴ J. W. Cahn, Acta Metall. **9**, 795 (1961); Trans. Metall. Soc. AIME **242**, 166 (1968).

⁵ J. Tersoff, Phys. Rev. Lett. **85**, 2843 (2000).

⁶ P. Venezuela and J. Tersoff, Phys. Rev. B **58**, 10871 (1998).

⁷ J. Tersoff, Phys. Rev. Lett. **77**, 2017 (1996).

⁸ J. E. Guyer and P. W. Voorhees, Mat. Res. Soc. Symp. Proc. **399**, 351 (1996).

⁹ J. E. Guyer and P. W. Voorhees, Phys. Rev. B **54**, 11710 (1996).

- ¹⁰ J. E. Guyer and P. W. Voorhees, Phys. Rev. Lett. **74**, 4031 (1995).
- ¹¹ J. E. Guyer and P. W. Voorhees, J. Cryst. Growth **187**, 150 (1998).
- ¹² B. J. Spencer, P. W. Voorhees, and J. Tersoff, Phys. Rev. B, **64**, 235318 (2001).
- ¹³ B. J. Spencer, P. W. Voorhees, and J. Tersoff, Appl. Phys. Lett. **76**, 3022 (2000).
- ¹⁴ B. J. Spencer, P. W. Voorhees, and J. Tersoff, Phys. Rev. Lett. **84**, 2449 (2000).
- ¹⁵ B. J. Spencer, P. W. Voorhees, and S. H. Davies, J. Appl. Phys. **73**, 4955 (1993).
- ¹⁶ B. J. Spencer, P. W. Voorhees, and S. H. Davis, Phys. Rev. Lett. **67**, 3696 (1991).
- ¹⁷ F. Glas, Phys. Rev. B **55**, 11277 (1997).
- ¹⁸ F. Léonard and R. C. Desai, Appl. Phys. Lett. **74**, 40 (1999).
- ¹⁹ F. Léonard and R. C. Desai, Appl. Phys. Lett. **73**, 208 (1998).
- ²⁰ F. Léonard and R. C. Desai, Phys. Rev. B **57**, 4805 (1998).
- ²¹ F. Léonard and R. C. Desai, Phys. Rev. B **56**, 4955 (1997).
- ²² F. Léonard and R. C. Desai, Phys. Rev. B **55**, 9990 (1997).
- ²³ Y. H. Xie, G. H. Gilmer, C. Roland, P. J. Silverman, S. K. Buratto, J. Y. Cheng, E. A. Fitzgerald, A. R. Kortan, S. Schuppler, M. A. Marcus, and P. H. Citrin, Phys. Rev. Lett. **73**, 3006 (1994).
- ²⁴ D. E. Jesson, S. J. Pennycook, J. Z. Tischler, J. D. Budai, J.-M. Baribeau, and D. C. Houghton, Phys. Rev. Lett. **70**, 2293 (1993).
- ²⁵ C. Schelling, G. Springholz, and F. Schaffler, Thin Solid Films **380**, 20 (2000).
- ²⁶ D. D. Perović, B. Bahierathan, H. Lafontaine, D. C. Houghton, and D. W. McComb, Physica A **239**, 11 (1997).
- ²⁷ P. Sutter and M. G. Lagally, Phys. Rev. Lett. **84**, 4637 (2000).
- ²⁸ R. M. Tromp, F. M. Ross and M. C. Reuter, Phys. Rev. Lett. **84**, 4641 (2000).
- ²⁹ T. Walther, C. J. Humphreys, and A. G. Cullis, Appl. Phys. Lett. **71**, 809 (1997).
- ³⁰ C. W. Snyder, B. G. Orr, D. Kessler, and L. M. Sander, Phys. Rev. Lett. **66**, 3032 (1991).
- ³¹ T. Okada, G. C. Weatherly, and D. W. McComb, J. Appl. Phys. **81**, 2185 (1997).
- ³² F. Peiró, A. Cornet, J. R. Morante, A. Georgakilas, C. Wood, and A. Christou, Appl. Phys. Lett. **66**, 2391 (1995).
- ³³ D. González, G. Aragón, D. Araújo, and R. Garcia, Appl. Phys. Lett. **76**, 3236 (2000).
- ³⁴ J. E. Guyer, S. A. Barnett, and P. W. Voorhees, J. Crystal Growth **217**, 1 (2000).
- ³⁵ M. Gendry, G. Grenet, Y. Robach, P. Krapf, L. Porte, and G. Hollinger, Phys. Rev. B **56**, 9271 (1995).
- ³⁶ N. Grandjean, J. Massies, M. Leroux, J. Leymarie, A. Vasson, and A. M. Vasson, Appl. Phys. Lett. **64**, 2664 (1994).
- ³⁷ N. S. Chokshi and J. M. Millunchick, Appl. Phys. Lett. **76**, 2382 (2000).
- ³⁸ F. K. LeGoues, M. Copel, and R. M. Tromp, Phys. Rev. B **42**, 11690 (1990).
- ³⁹ A. Ballestad, B. J. Ruck, M. Adamcyk, T. Pinnington, and T. Tiedje, Phys. Rev. Lett. **86**, 2377 (2001).
- ⁴⁰ Q. Xie, A. Madhukar, P. Chen, and N. P. Kobayashi, Phys. Rev. Lett. **75**, 2542 (1995).
- ⁴¹ F. C. Larché and J. W. Cahn, Acta Metall. **33**, 331 (1985).
- ⁴² S. J. Chey and D. G. Cahill, in *Dynamics of Crystal Surfaces and Interfaces*, edited by Duxbury and Pence (Plenum Press, New York, 1997), p. 59.
- ⁴³ The surface reconstruction effects considered here mainly apply to the ultra-high vacuum growth like MBE, while for the growing processes under hydrogen environment, such as CVD, the dimer formation is prevented due to the passivation effect of hydrogen on the dangling bonds, and then the corresponding diffusion kinetics are different from that discussed in this paper. See, e.g., C. S. Ozkan, W. D. Nix, and H. Gao, Mat. Res. Soc. Symp. Proc. **440**, 323 (1997).
- ⁴⁴ H.J.W. Zandvliet, B. Poelsema, and B.S. Swartzentruber, Physics Today **54**, 40 (July 2001).
- ⁴⁵ X. R. Qin, B. S. Swartzentruber, and M. G. Lagally, Phys. Rev. Lett. **85**, 3660 (2000).
- ⁴⁶ F. Léonard and R. C. Desai, Thin Solid Films **357**, 46 (1999).
- ⁴⁷ Z. F. Huang and R. C. Desai, Phys. Rev. B, in press.
- ⁴⁸ In general the roughness of the film-substrate interface may necessitate its location at $z = \zeta(x, y)$ instead of at $z = 0$. We have investigated whether a nonzero ζ contributes to any instability at the top surface $z = h(x, y)$, using the general solution of mechanical equilibrium equation in Appendix A. Our conclusion is that an undulation at the film-substrate interface results in an exponentially damped perturbation at top surface as the film grows and is thus benign.
- ⁴⁹ W. W. Mullins, J. Appl. Phys. **28**, 333 (1957).
- ⁵⁰ M. Atzmon, D. A. Kessler, and D. J. Srolovitz, J. Appl. Phys. **72**, 442 (1992).
- ⁵¹ P. Kumar and K. Maki, Phys. Rev. B **13**, 2011 (1976).
- ⁵² We have also studied the case where γ may have a linear composition dependence and found that it has no extra contribution to the results of linear stability analysis.
- ⁵³ J. W. Cahn and J. E. Hilliard, J. Chem. Phys. **28**, 258 (1958).
- ⁵⁴ A. Onuki and A. Furukawa, Phys. Rev. Lett. **86**, 452 (2001).
- ⁵⁵ More precisely, the functional differentiation of free energy functional \mathcal{F} with respect to ϕ generates an extra contribution proportional to $\delta(z - h)$ (mostly caused by u_{ij}^{hom}), corresponding to an additional boundary condition for compositional variable at surface $z = h$ which is not relevant in linear analysis.

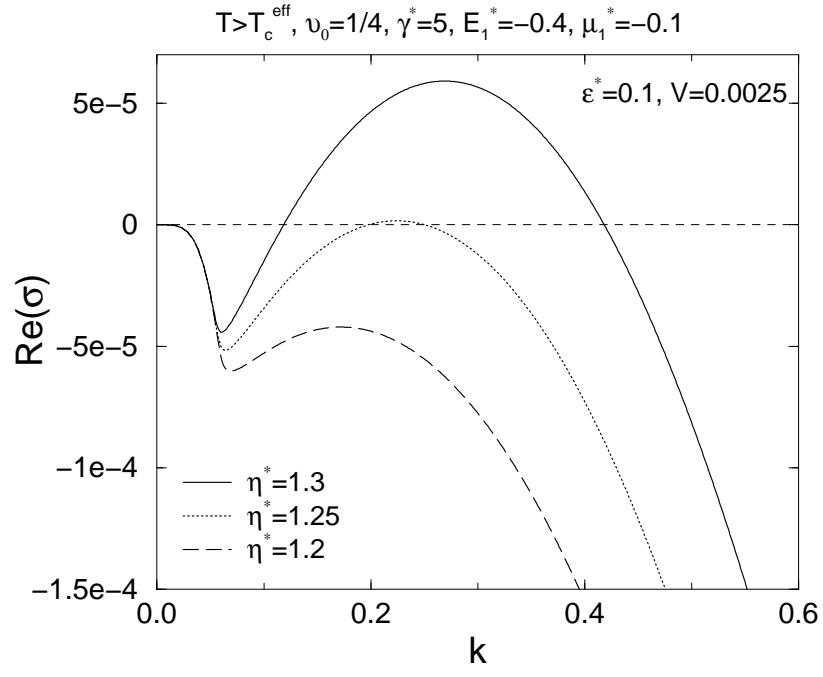


FIG. 1: Dispersion relation for real part of perturbation growth rate σ versus wavenumber k .

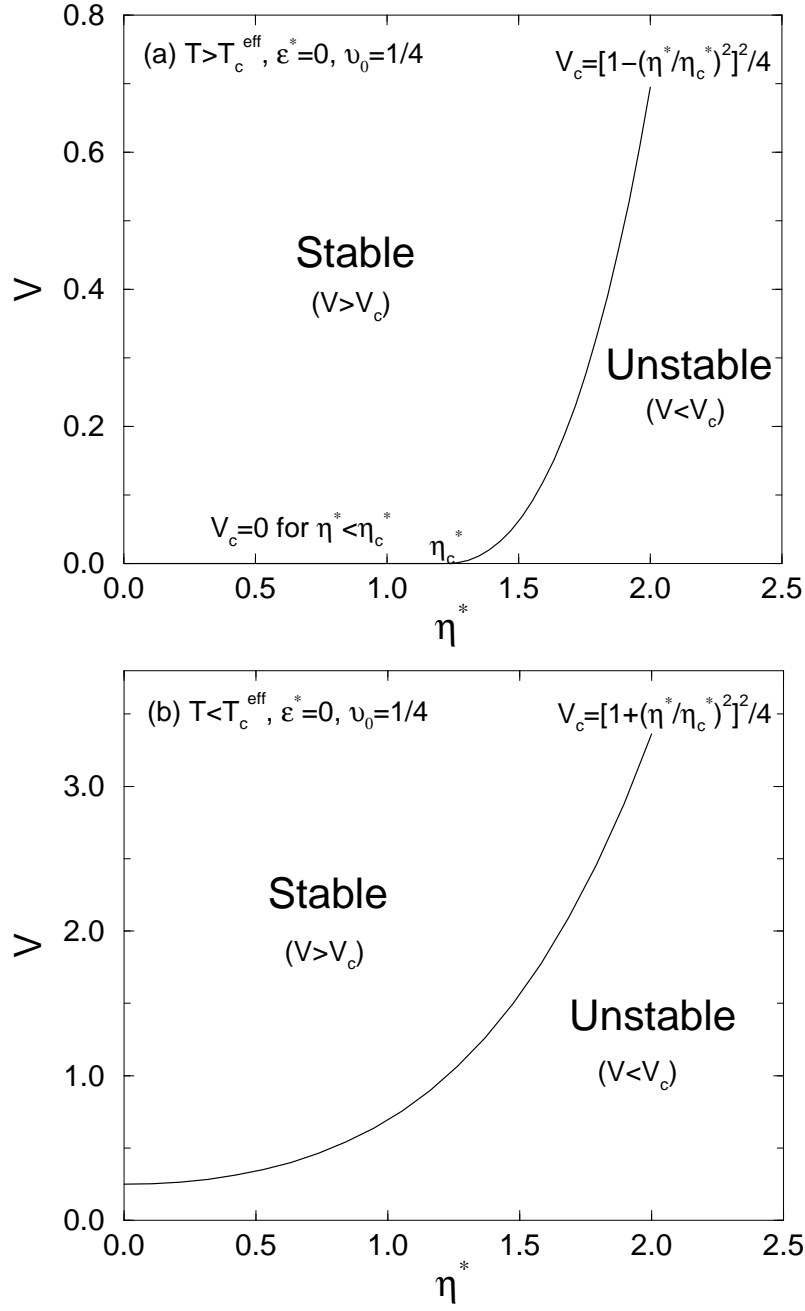


FIG. 2: Stability diagrams of rescaled deposition rate V versus η^* , for special case of no misfit $\epsilon^* = 0$, $\nu_0 = 1/4$, as well as growth temperature (a) $T > T_c^{\text{eff}}$ and (b) $T < T_c^{\text{eff}}$. These diagrams are calculated from the analytic results given in Eqs. (47) and (48).

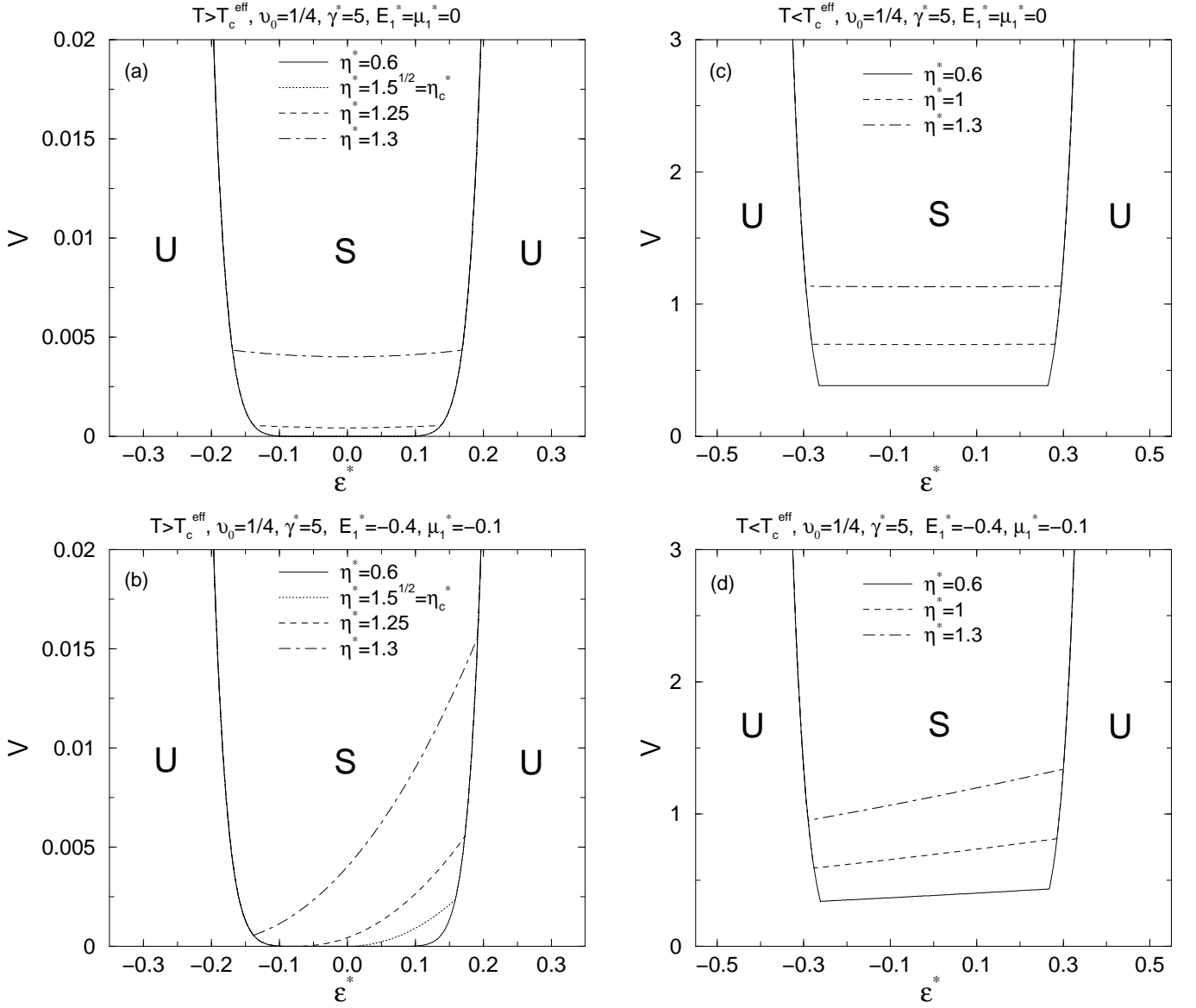


FIG. 3: Stability diagrams of deposition rate V versus misfit ϵ^* , with SiGe-like parameters $\nu_0 = 1/4$, $\gamma^* = 5$, and different cases of composition independent ((a) and (c): $E_1^* = \mu_1^* = 0$) or composition dependent ((b) and (d): $E_1^* = -0.4$, $\mu_1^* = -0.1$) elastic moduli. (a) and (b) correspond to $T > T_c^{\text{eff}}$ systems, while (c) and (d) are for $T < T_c^{\text{eff}}$. Stable and unstable regions are marked as “S” and “U”, respectively. η^* values increase from bottom to top stability boundary lines, as indicated in the figures, and in figure (a) all curves with $\eta^* \leq \eta_c^* = 1.5^{1/2}$ cannot be distinguished from each other for the scale plotted here. Note that the vertical scales of V in (c) and (d) for $T < T_c^{\text{eff}}$ are much larger than those of (a) and (b) for $T > T_c^{\text{eff}}$.

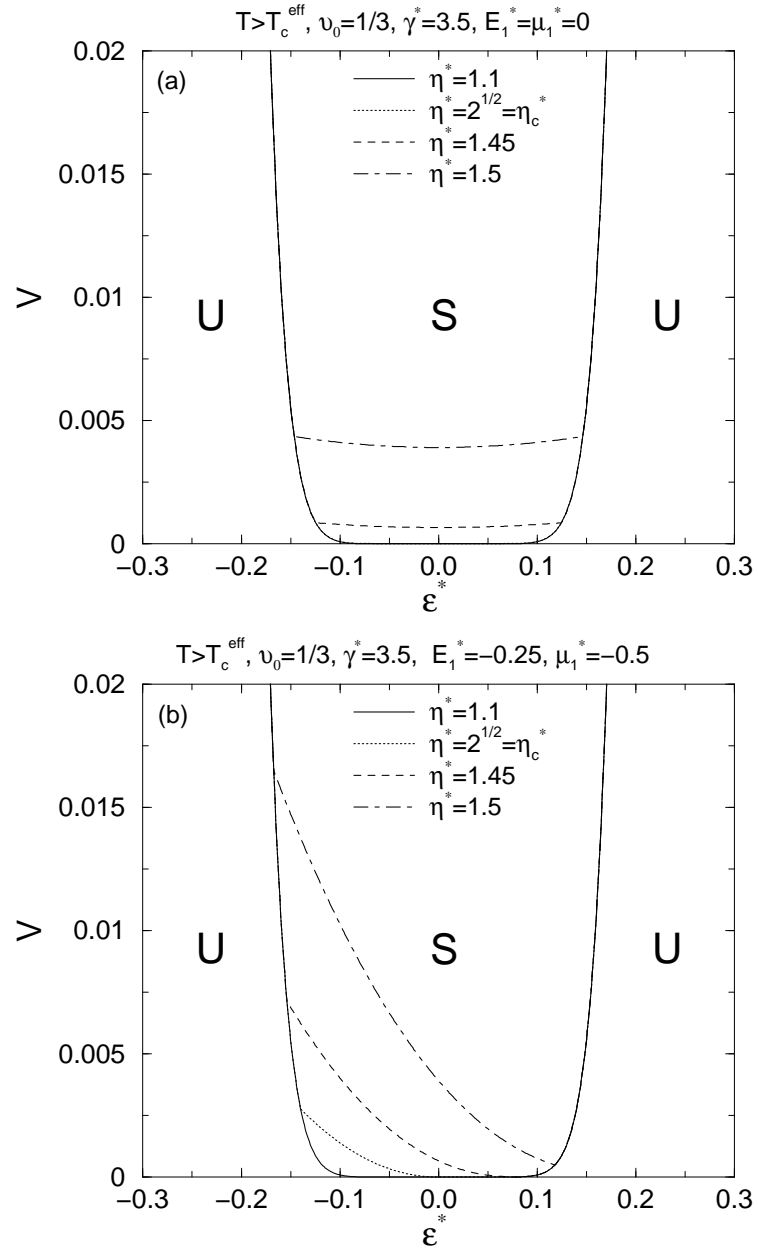


FIG. 4: Stability diagrams of deposition rate V versus misfit ϵ^* similar to Fig. 3, except for $T > T_c^{\text{eff}}$ and for InGaAs-like parameters $\nu_0 = 1/3$, $\gamma^* = 3.5$, $\eta_c^* = 2^{1/2}$, as well as $E_1^* = -0.25$ and $\mu_1^* = -0.5$. Compared with Fig. 3, different asymmetry with respect to sign of misfit ϵ^* is shown for (b), due to different material parameters. The diagrams for $T < T_c^{\text{eff}}$ (not shown here) are similar to those of Fig. 3, except the opposite asymmetry for nonzero E_1^* and μ_1^* .

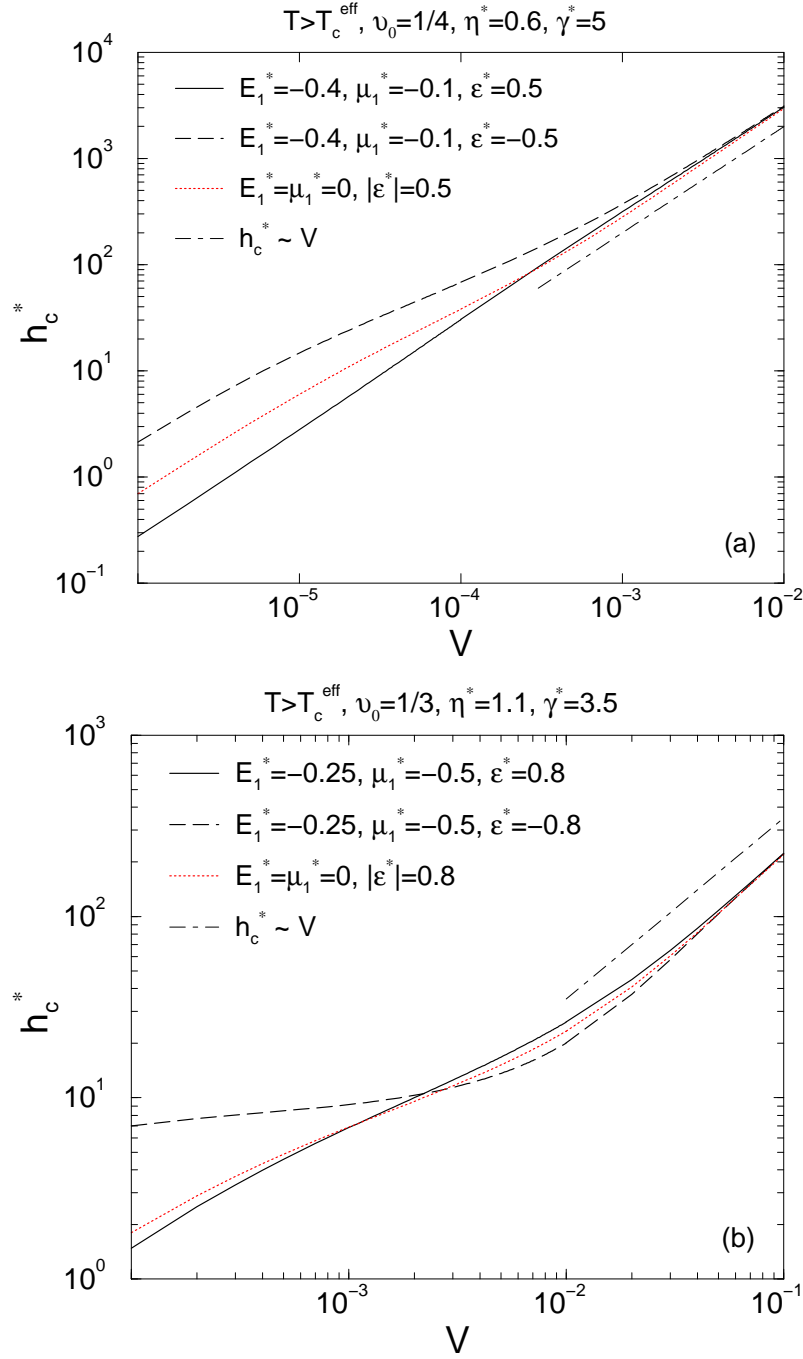


FIG. 5: Kinetic critical thickness (nondimensional) h_c^* as a function of rescaled deposition rate V for growth temperature above T_c^{eff} . The solid ($\epsilon^* > 0$) and dashed ($\epsilon^* < 0$) curves are for the case of composition dependent elastic moduli, while the dotted curve represents the result for composition independent moduli. The dot-dashed line of linear relationship $h_c^* \propto V$ is also drawn for comparison. (a) The material parameters are chosen to qualitatively represent the SiGe-like film: $\nu_0 = 1/4$, $\eta^* = 0.6$, $\gamma^* = 5$, $E_1^* = -0.4$, $\mu_1^* = -0.1$, and $|\epsilon^*| = 0.5$; (b) The parameters are expected to qualitatively represent the InGaAs-like alloy: $\nu_0 = 1/3$, $\eta^* = 1.1$, $\gamma^* = 3.5$, $E_1^* = -0.25$, $\mu_1^* = -0.5$, and $|\epsilon^*| = 0.8$.

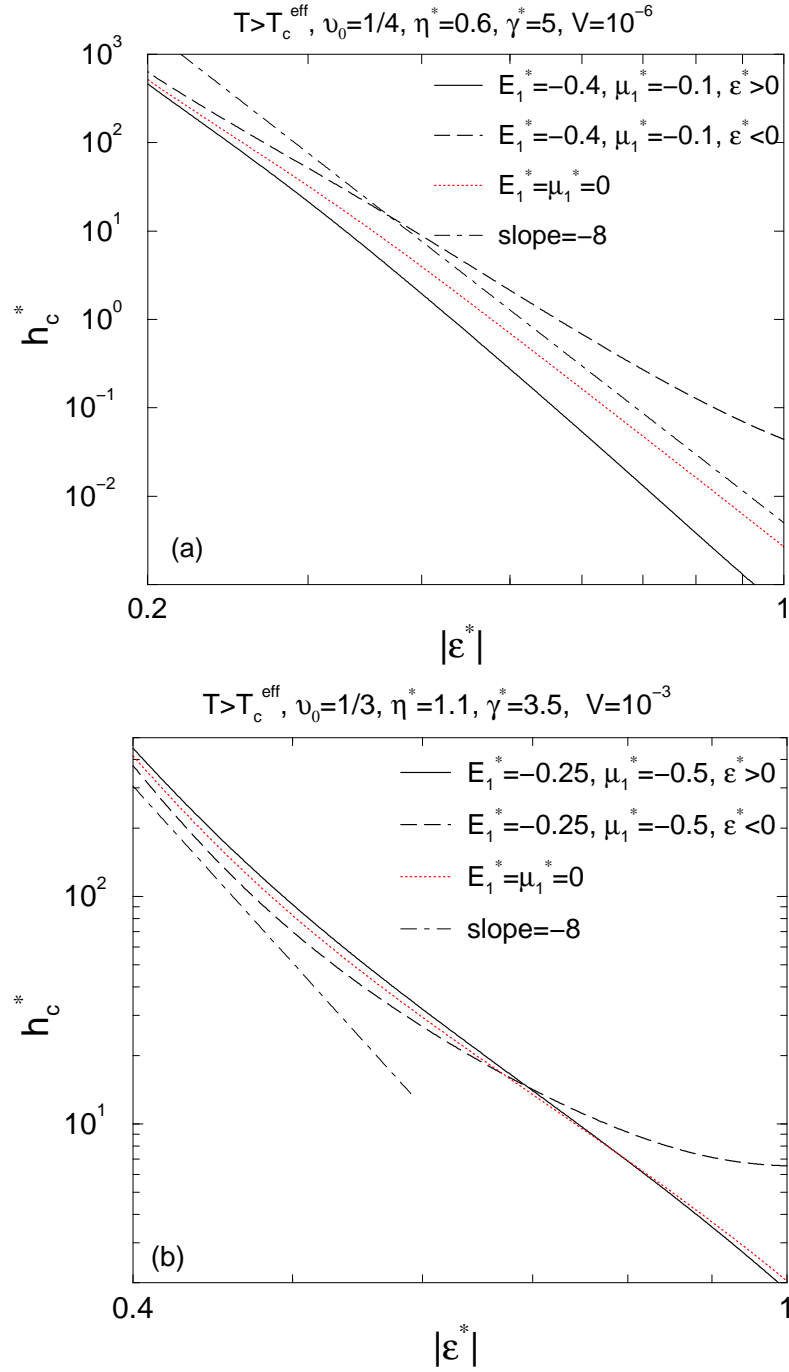


FIG. 6: Rescaled kinetic critical thickness h_c^* as a function of absolute value of rescaled misfit strain $|\epsilon^*|$ for temperature $T > T_c^{\text{eff}}$. Similar to Fig. 5, the solid and dashed curves are for positive and negative misfit ϵ^* respectively, with composition dependent elastic moduli, while the dotted curve corresponds to the case of composition independent moduli. The dot-dashed line represents the power law scaling behavior with exponent -8 , which is used for comparison. In (a), the rescaled deposition rate is chosen as $V = 10^{-6}$, and in (b) it is $V = 10^{-3}$. All the other parameters are the same as those in Fig. 5.